

Crossmark

RESEARCH PAPER - PREPRINT

RECEIVED
dd Month yyyy
REVISED
dd Month yyyy

Pure and Physics-Guided Deep Learning Solutions for Spatio-Temporal Groundwater Level Prediction at Arbitrary Locations

Matteo Salis^{1,3,*}, Gabriele Sartor¹, Rosa Meo¹, Stefano Ferraris², Abdourrahmane M. Atto³

¹Computer Science Department, University of Turin, Turin, Italy

²Interuniversity Department of Regional and Urban Studies and Planning, Politecnico di Torino and University of Turin, Turin, Italy

³LISTIC Laboratory, Université Savoie Mont Blanc, Annecy-le-vieux, France

*Corresponding author.

E-mail: matteo.salis@unito.it or salis.matteo98@gmail.com (corresponding author)

Keywords: Physics-Guided Machine Learning, Spatio-Temporal Data, Geospatial AI, Groundwater, Hydrology

Abstract

Groundwater represents a key element of the water cycle, yet it exhibits intricate and context-dependent relationships that make its modeling a challenging task. Theory-based models have been the cornerstone of scientific understanding. However, their computational demands, simplifying assumptions, and calibration requirements limit their use. In recent years, data-driven models have emerged as powerful alternatives. In particular, deep learning has proven to be a leading approach for its design flexibility and ability to learn complex relationships.

We proposed an attention-based pure deep learning model, named STAINet, to predict weekly groundwater levels at an arbitrary and variable number of locations, leveraging both spatially sparse groundwater measurements and spatially dense weather information. Then, to enhance the model's trustworthiness and generalization ability, we considered different physics-guided strategies to inject the groundwater flow equation into the model. Firstly, in the STAINet-IB, by introducing an inductive bias, we also estimated the governing equation components. Then, by adopting a learning bias strategy, we proposed the STAINet-ILB, trained with additional loss terms adding supervision on the estimated equation components. Lastly, we developed the STAINet-ILRB, leveraging the groundwater body recharge zone information estimated by domain experts.

The STAINet-ILB performed the best, achieving overwhelming test performances in a roll-out setting (median MAPE 0.16%, KGE 0.58). Furthermore, it predicted sensible equation components, providing insights into the model's physical soundness. Physics-guided approaches represent a promising opportunity to enhance both the generalization ability and the trustworthiness, thereby paving the way to a new generation of disruptive hybrid deep learning Earth system models.

1 Introduction

In recent years, deep learning models have achieved striking results in modeling many natural phenomena, including water resources [1, 2, 3, 4]. However, good predictions in terms of accuracy and precision are not enough. In some contexts, it is pivotal to have models that are not only able to replicate observed data but truly understand the generating process under study. Furthermore, black-box approaches can be challenging to employ when the goal is to advance scientific understanding or support binding decision-making, given the lack of interpretation of what they have learned [5]. This poses major concerns in critical and high-stakes applications (e.g., natural hazards, healthcare, legal domain, etc.).

One of the primary issues in studying hydrological and, more generally, environmental phenomena is the limited availability and quality of data. Indeed, environmental datasets are often incomplete, and labelled instances may fail to capture the full complexity of the underlying systems. Natural processes often exhibit intricate, non-stationary dynamics that evolve over time, influenced also by

arXiv:2603.25779v1 [cs.LG] 26 Mar 2026

exogenous factors (e.g., climate change). Thus, inferring future trends from past observations might not be effective in some circumstances, because the process could change following unseen patterns – a situation well illustrated by the inductivist turkey¹. For this reason, data-driven approaches, especially for environmental applications, might easily focus on spurious associations, making models unable to generalize well over the available spatio-temporal domain of the observations [5, 6].

Until now, theory-based models have been the milestone for our scientific knowledge and discovery. Briefly, theory-based approaches are based on cause-and-effect relationships, either empirically proven or theoretically demonstrated, starting from some postulates. Some examples are closed-form equations (e.g., continuity equations) or computational simulations of dynamical systems described by differential equations (e.g., Richards and Navier-Stokes equations). Although theory-based models remain invaluable for advancing our understanding of natural systems, they often rely on simplifying assumptions either because of incomplete knowledge of certain processes or to make the model computationally tractable. However, these assumptions are not always guaranteed in nature, and observations may diverge from model simulations [5, 7]. Furthermore, many internal parameters are usually required and thus estimated for the specific application, a procedure usually named model calibration. To calibrate a model, many observations are required; however, it is not always feasible to obtain such data, either because of the expensive measurements or observational restrictions. This leads again to simplifying assumptions that may cause the model performance limitations [8, 5, 9, 10, 7].

Given that theory-based and data-driven approaches have their own advantages and disadvantages, a consistent number of researchers have proposed a mixed strategy to leverage the strengths of both, i.e., theory-guided data science [5, 6, 7], and specifically for physics and machine learning, the physics-guided (or informed) machine learning [11, 12, 13]. The idea is to inject prior scientific knowledge, a bias (or guidance), into a data-driven model, and to this aim, several approaches have been proposed, which differ in where to place the bias into the modeling pipeline. In general, three main strategies can be identified [12, 13]: observational bias, inductive bias, and learning bias.

The observational bias strategy is conceptually the simplest one, as it simply assumes that the data considered truly and completely represent the underlying physical process. This could be achieved either by using accurate ground measurement, but as already pointed out, measurements could be scarce and costly, or by augmenting data with theory-based simulation [14].

The second strategy, the inductive bias, consists of designing the data-driven model in a way that implicitly embeds the domain knowledge. In the case of neural networks, it means developing specific layers that strictly enforce the desired relation. For example, as presented in [15] to enforce the advection-diffusion equation on sea-surface temperature data, and in [16] to find the viscosity solutions of two sets of Hamilton–Jacobi partial differential equations. Even though this strategy can constrain the model to strictly adhere to the domain prior, it requires ad hoc implementation, and usually, only simple and well-defined equations are injected [13].

The third strategy is the most general one, and it involves adding to the loss function between true and predicted data (\mathcal{L}_{data}) some regularization terms (\mathcal{L}_{eq}) related to the residuals of the prior governing equation with respect to the model output. In general, the governing equation that describes the evolution of a phenomenon is expressed as a Partial Differential Equation (PDE). Within this framework, the model is trained to fit both the observed data and the physical constraints imposed by domain knowledge. This approach exploits the universal approximation capability of neural networks, enabling them to approximate PDE solutions leveraging automatic differentiation, and without requiring explicit domain discretization [11, 17]. Neural architectures designed for this purpose are commonly referred to in the literature as Physics-Informed Neural Networks (PINNs) [11]. The advantages of this last approach are: **a)** the neural network can be trained on the loss related to the prior equation (\mathcal{L}_{eq}) with limited (or even any) labelled data; and **b)** if the differential equation contains some unknown parameters, these could be jointly estimated with the model’s own parameters during the training process. However, given that the prior is injected as a regularization term into the loss, the model is not strictly, but softly bound to the domain knowledge, and thus could produce output not completely adhering to the prior equation.

Although all three strategies have been demonstrated to be effective, the inductive and learning biases are the most adopted in recent years [12, 13, 6], the former because of the possibility of introducing hard constraints, the latter for its flexibility.

In our application, we focused on groundwater, one of the major freshwater components in the water-cycle, whose accurate accounting is critical for water policy planning, especially in the presence

¹The inductive turkey (also known as the turkey illusion) exemplifies the problem of induction, originally described by Bertrand Russell in *The Problems of Philosophy*. It tells of a turkey that, being fed daily, infers that this pattern will persist indefinitely—until, on the day before Thanksgiving, it is slaughtered, exposing the weakness of its assumption.

of climate change.

In more detail, this work addressed two main objectives. Firstly, we aimed to model the weekly groundwater level in Piedmont (Italy), evaluating different strategies for the injection of the groundwater flow equation. Additionally, given our interest in developing a general model for the whole Area of Interest (ROI), we sought to build models able to predict at any desired (i.e., arbitrary) location all over the ROI, leveraging an autoregressive and an exogenous component, which consist of the spatially sparse groundwater measurements derived from in situ sensors (piezometers) and the spatially dense, or distributed, weather information (weather video). To the best of our knowledge, this is the first study to test different physics-guided deep learning approaches in a real-world scenario, rather than on simulated groundwater data.

1.1 Groundwater principles

Our study addressed the shallow groundwater bodies, named also phreatic aquifers or unconfined aquifers, which are portions of the terrain saturated with water and directly influenced by the superficial activity, and whose upper surface, denoted as the water table, is at atmospheric pressure. To quantify groundwater resources, the groundwater level (GWL) is frequently adopted, and it represents the distance between the reference datum and the water table.

Groundwater dynamics are usually described by using Darcy’s law, which states that the specific discharge q_x in the x -direction is proportional to the gradient of the total hydraulic head h multiplied by the saturated hydraulic conductivity K_x . More specifically, the specific discharge q_x is the volume rate of flow per unit of area, and the hydraulic head is the potential mechanical energy per unit weight of fluid. The hydraulic head is the sum of the gravitational head, given by the elevation of the point above an arbitrary horizontal datum, and the pressure head, which is the pressure of the fluid at the point divided by the specific weight of the fluid. In the case of an unconfined aquifer, whose upper surface is at atmospheric pressure, the hydraulic head is equivalent to the water table height (i.e., groundwater level). Therefore, it is possible to write Darcy’s law as in Equation 1:

$$q_x = -K_x \frac{\partial h}{\partial x} \quad (1)$$

Combining Darcy’s law with the mass conservation principle, it is possible to derive a general PDE, a form of diffusion equation, for the saturated groundwater flow in the three spatial dimensions (x, y, z) , as in Equation (2). The term S_s represents the specific storage² [L⁻¹], that is the volume of water entering/leaving from a unit volume per unit variation in hydraulic head, and K_x, K_y, K_z are the conductivity in the specific directions, all expressed in [LT⁻¹].

$$\frac{\partial h}{\partial t} S_s = K_x \frac{\partial^2 h}{\partial x^2} + K_y \frac{\partial^2 h}{\partial y^2} + K_z \frac{\partial^2 h}{\partial z^2} \quad (2)$$

However, attention is typically directed toward horizontal flow along the aquifer plane of coordinates (x, y) . Considering a simplified formulation and defining the transmissivity $T = H \cdot K$ [L²T⁻¹] and the storage coefficient $S = H \cdot S_s$ [1], in which H [L] is the saturated thickness of the aquifer and K is the horizontal conductivity, it is possible to define the groundwater flow equation for the horizontal flow (hereafter groundwater flow equation) as in Equation (3):

$$\frac{\partial h}{\partial t} S = T \left(\frac{\partial^2 h}{\partial x^2} + \frac{\partial^2 h}{\partial y^2} \right) \quad (3)$$

We reformulated Equation (3), moving S to the right-hand side obtaining Equation (4). The resulting quantity $\frac{T}{S}$ is related to the ease with which water moves through the soil, and it is expressed in [L²T⁻¹].

$$\frac{\partial h}{\partial t} = \frac{T}{S} \left(\frac{\partial^2 h}{\partial x^2} + \frac{\partial^2 h}{\partial y^2} \right) \quad (4)$$

2 Related Works

An increasing number of studies have explored the implementation of physics-guided approaches across a wide range of domains, including healthcare [18, 19], computer vision [20], geoscience [15, 21, 22, 23], weather [24, 25], air-pollution [26], and hydrology [27, 22, 28, 29].

²As common in hydrology, to describe a unit of measurement, we adopted the terminology of the fundamental physical dimensions, thus length [L] and time [T] – in our case meters [m] and weeks [w]

More in detail, the work presented in [15] aimed to develop a deep learning model to predict sea surface temperature in an autoregressive fashion, leveraging the information of the advection-diffusion equation and adopting both inductive and learning bias strategies. The authors developed a specific architecture made of two branches. The first, made of a U-Net-like structure, explicitly estimates the motion field; the second enforces the motion field on the last available temperature image through a mathematically consistent warping scheme. The warping scheme was developed to obtain the demonstrated discretized solution using a radial basis function kernel (inductive bias). The relevant point in this work is that there is no direct supervision on the motion vector field, but only a weak supervision through some regularization terms added to the final loss (learning bias). With this model, the authors achieved better performance than a numerical assimilation model and other deep learning implementations, proving the effectiveness of their solution.

Concerning hydrology, the inductive bias strategy was adopted in [27] to develop a physics-guided neural network with the aim of modeling runoff across the conterminous United States. In particular, they proposed an architecture comprising two consecutive blocks. The first is composed of a restructured version of an RNN layer, named P-RNN, which embeds the spatially lumped hydrological model described by two discrete state-space representations. Then the second block, made of usual 1D convolutional layers, takes the original input along with the P-RNN output to model the residual component with respect to the physics. The proposed physics-guided model achieved better performance compared to other deep learning implementations.

A different strategy was followed by authors in [28, 29]. Indeed, they adopted the PINNs approach (learning bias) to estimate groundwater flow simulated data. In the first study [28], a multilayer-perceptron (MLP) was trained to estimate the solution of the groundwater flow equation in one and two-dimensional cases in the presence of pumping wells, by adding to the loss a residual term of the PDE and boundary condition terms. The trained PINN was revealed to be more accurate than the finite difference method adopted as a comparison. In the second study [29], the authors aimed to estimate the phreatic surface (i.e., water-table) and the piezometric heads in a vertical cross-section of a homogeneous and isotropic aquifer and a heterogeneous and anisotropic one. To this aim, they proposed a physics-informed neural network made of two sub-networks, each implemented as an MLP. The first is responsible for estimating the piezometric head value along the vertical cross-section over time, while the second network is designed to predict the phreatic surface. In that study, MODFLOW [30] simulations were performed and considered as the true data in the training process, jointly with the residuals of the groundwater flow equation. Even though the architecture appears to be intricate, the authors achieved better performance than a pure deep learning architecture without the physics loss. Furthermore, they highlighted the ability of PINNs to work in mesh-free domains (i.e., without discretization) and that incorporating physical constraints can dramatically reduce the number of required observations for training. This shows the PINNs' potential to generalize well also in data-scarce environments.

Even if these mentioned studies reveal the potential of a physics-guided deep learning approach, our application context is different. Indeed, in [15], the adopted target (sea surface temperature) is dense in space and time. This contrasts with our case, where groundwater level observations are spatially sparse, and predictions may be required at locations different from those of the input data. On the other hand, even if the PINN approach is flexible, it is usually implemented for theoretical analyses, and thus models are frequently developed to take as input only the coordinates of the system (spatial, temporal, or both), and less frequently exogenous, and real, inputs are considered. Furthermore, feeding multi-modal data (e.g., video and tabular data) to the models in this framework is non-immediate, and a careful design is needed.

In our study, to inject the groundwater flow equation, we implemented and tested two of the above mentioned strategies. Firstly, we introduced an inductive bias into the pure deep learning model by making the model estimate the different components of the governing equation. Afterwards, we added learning biases into the loss function to further condition the model.

Concerning our other objective of producing models that can predict at arbitrary spatial and temporal locations independently of the locations at which the input features are observed, we leveraged the attention mechanism [31]. Indeed, attention maps *values* indexed by *keys* to new values indexed by *queries* (in a database fashion), which offers a straightforward solution to leverage input data indexed by spatio-temporal coordinates (*keys*) to generate predictions at an arbitrary number of new locations (*queries*). Other works, as [3, 25], leverage spatially sparse data as well; however, in the first case [3] authors interpolated data into a grid, while in the second case [25], the authors adopted an MLP to perform the upsampling, and thus the number of input and output locations must be fixed in advance.

It is worth noting that developing models that automatically predict at different locations than

the input ones is in contrast with traditional approaches, which require input features to be co-located with the target variable and then use post hoc interpolation methods to generate predictions in new locations.

3 Data

In this study, we defined our ROI as a squared region with longitudes ranging from 6.6267° to 8.0292° and latitudes from 44.3108° to 45.2650°, of approximately 16700 km² (see Figure 1). In this area, we retrieved 28 piezometers’ weekly time series, measuring the groundwater level from 2001-01-01 to 2023-12-31. These sensors are part of the Regional Environmental Agency of Piedmont (ARPA Piemonte in Italian) network³. The time series of sensors in Cuneo, Racconigi, Scalenghe, and Vottignasco are reported in Figure 2; all the other time series, along with their means, standard deviations, and percentages of missing values, are shown in Section A in Figure 20 and Table 4. The right side of Figure 1 represents the location of all the sensors with a colour scale indicating their mean over time.

A visible aspect of these time series is that they show very different dynamics and missing periods. This is a complex issue to handle because it suggests the presence of different processes involved in the groundwater level data. In particular, some exogenous phenomena, like abstraction for irrigation or the response to precipitation, might act differently in different locations.

Given the high percentage of missing values among all sensors (see Table 4 in Section A) with an average value of around 23%, we decided not to discard any sensors but simply fill the missing data with the last available data for every sensor. These filled data were then masked out and thus not considered in the loss computation during training.

We adopted ERA5-land [32] as the source data for weather information. ERA5-land is a reanalysis dataset providing different environmental variables at a spatial resolution of 0.1° and an hourly temporal resolution. In particular, we downloaded total precipitation, 2 m height temperature, potential evaporation, and snowmelt, and performed a weekly average aggregation.

We considered data up to 2021-12-31 for training (around 90% of all instances), leaving data in 2022 and 2023 for testing (roughly 10%). Furthermore, we normalized all data by computing z-scores $z = \frac{F - \mu_F}{\sigma_F}$ for all features F , where all means μ_F and standard deviations σ_F were computed on the training set.

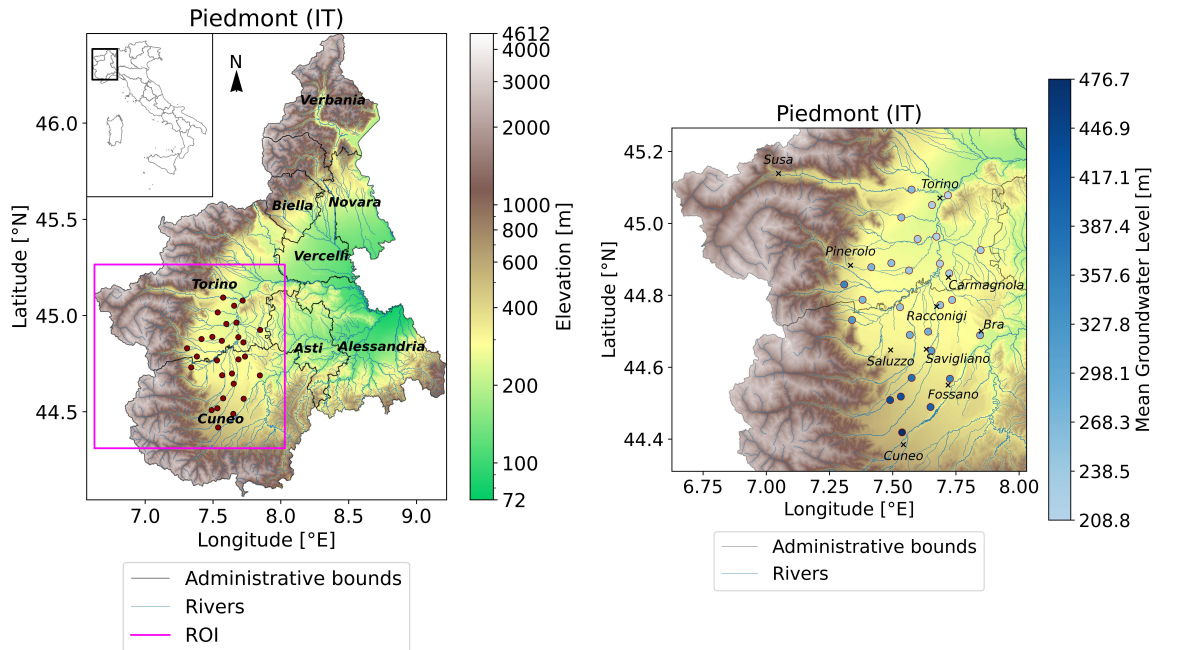


Figure 1: Piedmont region with the ROI box and the selected piezometers.

4 Methods

Our target variable is the hydraulic head $h(x, y, t)$ indexed by time t , and spatial coordinates x, y . Given that we considered the unconfined aquifer, h corresponds to the groundwater level (GWL)

³Free access is provided at <https://shorturl.at/F3KzQ>.

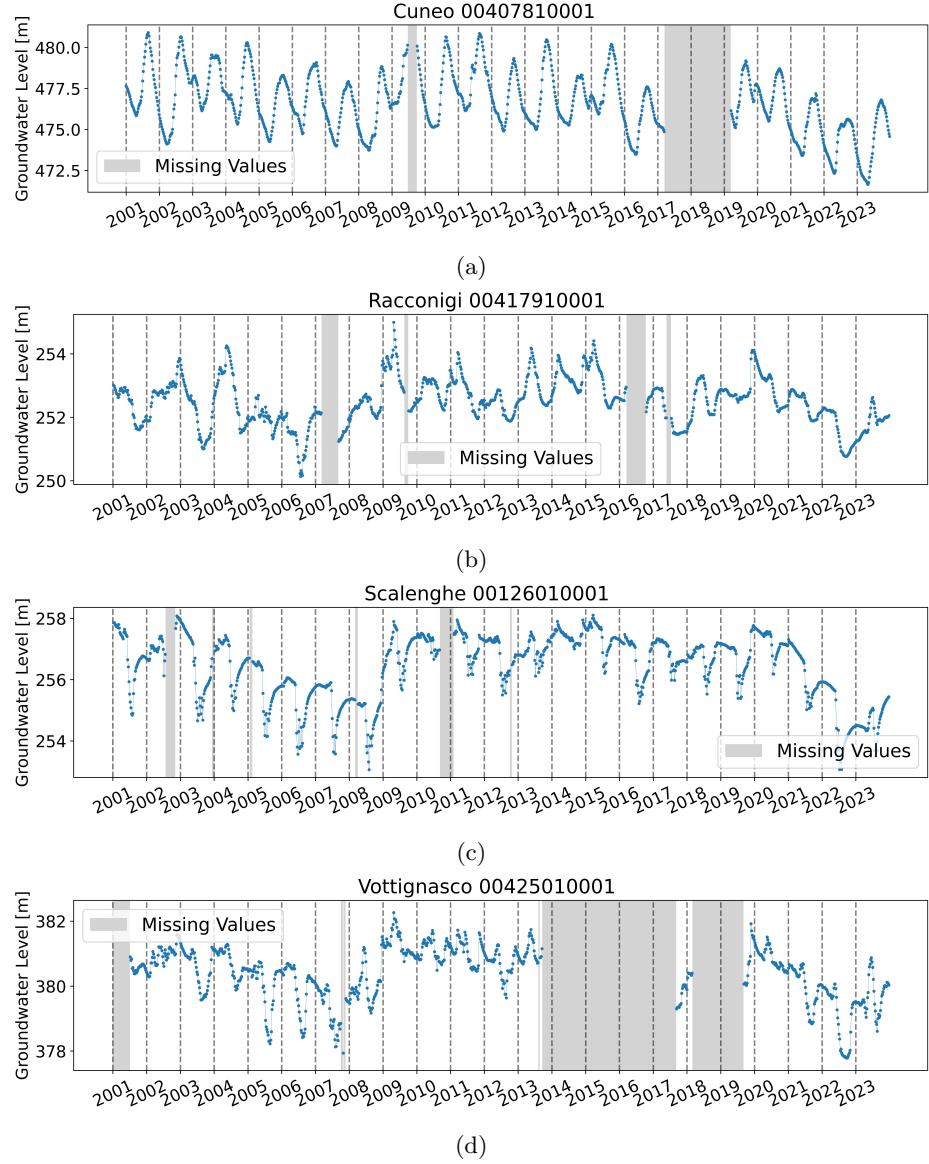


Figure 2: Time series of the sensors in **a)** Cuneo, **b)** Racconigi, **c)** Scalenghe, and **d)** Vottignasco.

measured by piezometers. The ROI, or spatial domain, is $\Omega \subset \mathbb{R}_{[ROI]}^2$ delimited by the bounding box defined by $(x_{min}, y_{min}), (x_{max}, y_{max})$. The piezometers measure h at $M = 28$ points inside the ROI, we can thus define the spatial measuring domain \mathcal{M} as the set of sensors' locations $\mathcal{M} = \{(x_m, y_m) | m \in [1; M]\}$ and $\mathcal{M} \subset \Omega$.

We aimed to develop a model that can predict an arbitrary number P of points \mathcal{P} inside the ROI at time t^* , more precisely $\mathcal{P} = \{(x_p, y_p) | p \in [1; P]\}$. Our target can thus be defined as $h_{\mathcal{P}, t^*} = \{h(x, y, t) | (x, y) \in \mathcal{P}, t = t^*\}$, note that $\mathcal{P} \subset \Omega$.

As input data, we leveraged an autoregressive component $H_{\mathcal{P}, t^*-1}$ made of \mathcal{T} lagged values of the target, i.e., $H_{\mathcal{P}, t^*-1} = \{h_{\mathcal{P}, t} | t \in [t^* - \mathcal{T}; t^* - 1]\}$. Furthermore, we used spatially dense weather data all over the ROI in the form of a video, from the time of the former \mathcal{T} lag up to the time t^* of the prediction. We defined the video as $\mathbf{V}_{t^*} = \{v(x, y, c, t) \in \mathbb{R} | (x, y) \in \mathcal{H} \times \mathcal{W}, c \in [1; \mathcal{C}], t \in [t^* - \mathcal{T}; t^*]\}$, where \mathcal{H}, \mathcal{W} are the horizontal and vertical centroids of each pixel of the video that covers the entire spatial domain Ω , and \mathcal{C} are the channels, i.e. total precipitation, 2 m height temperature, potential evaporation, and snowmelt.

Formally, $h_{\mathcal{P}, t^*} = f(H_{\mathcal{P}, t^*-1}, \mathbf{V}_{t^*}) + \epsilon_{\mathcal{P}, t^*}$ is the considered theoretical equation generating GWL data, where $\epsilon_{\mathcal{P}, t^*}$ is the irreducible error. The relation f can be approximated by a model f_{θ} parametrized by θ , in our case, a neural network.

4.1 Deep Learning Approach

4.1.1 Multi-Head Attention Mechanism To develop a deep learning model that leverages input data indexed by spatio-temporal coordinates and can generate predictions at an arbitrary and variable number of locations, we adopted the Multi-Head Attention (MHA) mechanism [31].

The MHA is based on the scaled dot-product attention that computes attention weights by taking the dot product between query (Q) and key (K) vectors, scaled by the inverse square root of the key dimension (d_k) to maintain numerical stability. These weights are normalized using a softmax function and applied to the corresponding value vectors (V) to produce a weighted sum representing the attention output (Equation 5). When the queries, keys, and values are all derived from the same input sequence, the mechanism is referred to as self-attention. This mechanism enables efficient computation of dependencies within a sequence by emphasizing relevant contextual information while mitigating gradient instability in high-dimensional spaces.

$$\text{Attention}(Q, K, V) = \text{softmax} \left(\frac{QK^T}{\sqrt{d_k}} \right) V \quad (5)$$

The Multi-Head formulation consists of performing n parallel and independent scaled dot-product attention (heads) on different linear transformations of the input query $Q_i = QW_i^Q$, value $V_i = VW_i^V$, and key $K_i = KW_i^K$ for $i \in [1; n]$. All heads' outputs are then concatenated, and a linear transformation is performed to produce the final output, as in Equation (6):

$$\text{Multi-Head Attention}(Q, K, V) = \text{Concat}(\text{head}_1, \dots, \text{head}_n)W^O \quad (6)$$

Where W_i^Q , W_i^V , W_i^K and W^O are learnable weight matrices, and the generic head $_i$ is equal to $\text{Attention}(Q_i, K_i, V_i)$.

This structure enables the model's capacity to extract different, but complementary, meaningful information from the input sequence and thus learning more complex relationships. The MHA layer is usually adopted in blocks, in which it is followed by feed-forward layers as in the Transformer architecture [31, 33].

For our purpose, and inspired by [33], we defined an MHA block as depicted in Figure 3a that consists of an MHA layer followed by an MLP made of two fully connected layers. We used the Instance Normalization [34] as the normalization procedure (Norm layer in Figure 3a), and LeakyReLU as the activation function after each layer. Two residual connections are then employed to ease the gradient flow.

4.1.2 Embedding Layers The values, keys, and queries were obtained through dedicated embedding layers. Conceptually, in our context, the keys or queries refer to the spatio-temporal coordinates of the input data and the prediction points, respectively. To create a more informative spatio-temporal coordinates embeddings (ST-CEmb), we augmented the coordinates (longitude and latitude) with the elevation, along with the sine and cosine signals of the day of the year (doy) as the temporal information – the functions $\sin(\frac{2\pi \text{doy}}{366})$ and $\cos(\frac{2\pi \text{doy}}{366})$ respectively. The usage of sine and cosine signals for the embedding creation has been adopted in the original Transformer architecture [31] to inform about the position of each token in the sequence, but also in environmental applications to ease the seasonality extraction [35, 36]. The augmented spatio-temporal coordinates of each point, either in input or to be predicted, were fed to a linear layer that gives in output the spatio-temporal coordinates embeddings – the keys, or the queries, respectively.

Concerning the computation of the spatio-temporal value embeddings (ST-VEmb), for the autoregressive component, we adopted a linear layer that takes as input the groundwater level value concatenated with the augmented spatio-temporal coordinates described before. Differently, for the value embedding of the weather data, we exploited the spatially dense nature of this input by feeding the weather features, concatenated with the augmented spatio-temporal coordinates, into a convolutional layer with a 3×3 kernel, followed by an average pooling layer. Consequently, the resulting ST-VEmb inherently captures the spatial structure of the meteorological variables.

4.1.3 Deep Learning Architecture Upon the MHA block, we defined **a**) the Spatio-Temporal Self-Attention (STSA, in Figure 3b) module made of one MHA block adopting self-attention; and **b**) the Spatio-Temporal Attention-based Interpolation (STAI, in Figure 3b) module composed of one MHA block in which the keys are the spatio-temporal coordinates embeddings of the input points, the values are the hidden representation of the value embeddings, and the queries are the spatio-temporal coordinates embeddings of the prediction points – given that the keys and queries could be of different lengths, we dropped the first residual connection in the MHA block.

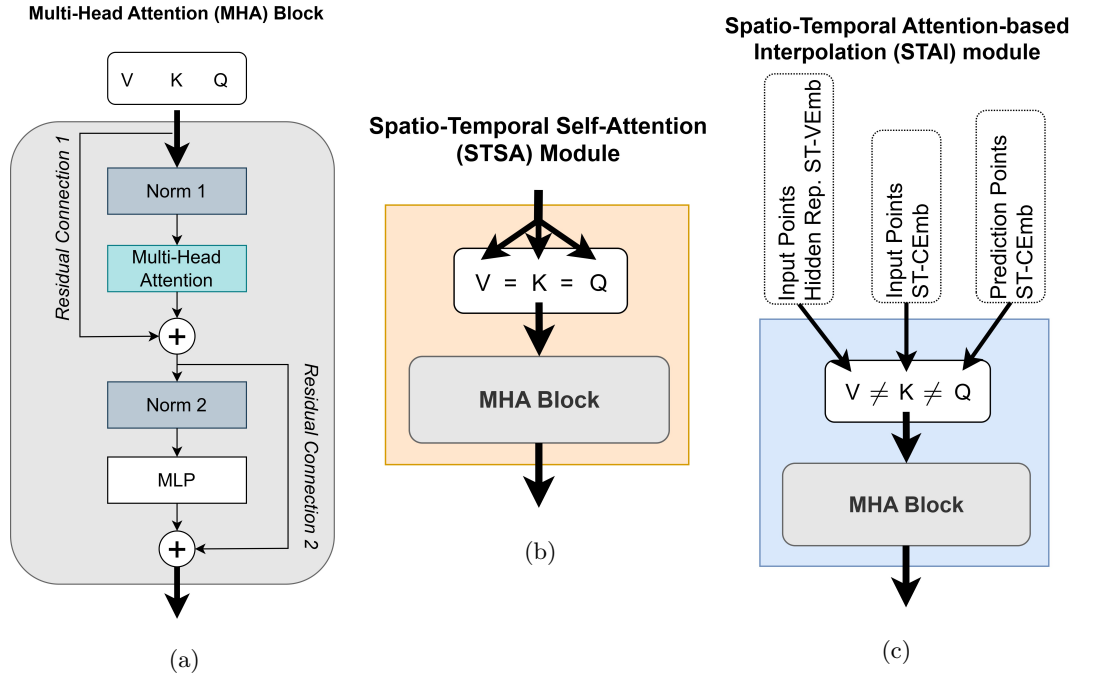


Figure 3: **a)** Multi-Head Attention block adopted in the models. **b)** STSA Module **c)** STAI Module that takes as values the input points hidden representation of the value embeddings, as keys the input points spatio-temporal coordinates embeddings (ST-CEmb), and as queries the prediction points spatio-temporal coordinates embeddings (ST-CEmb).

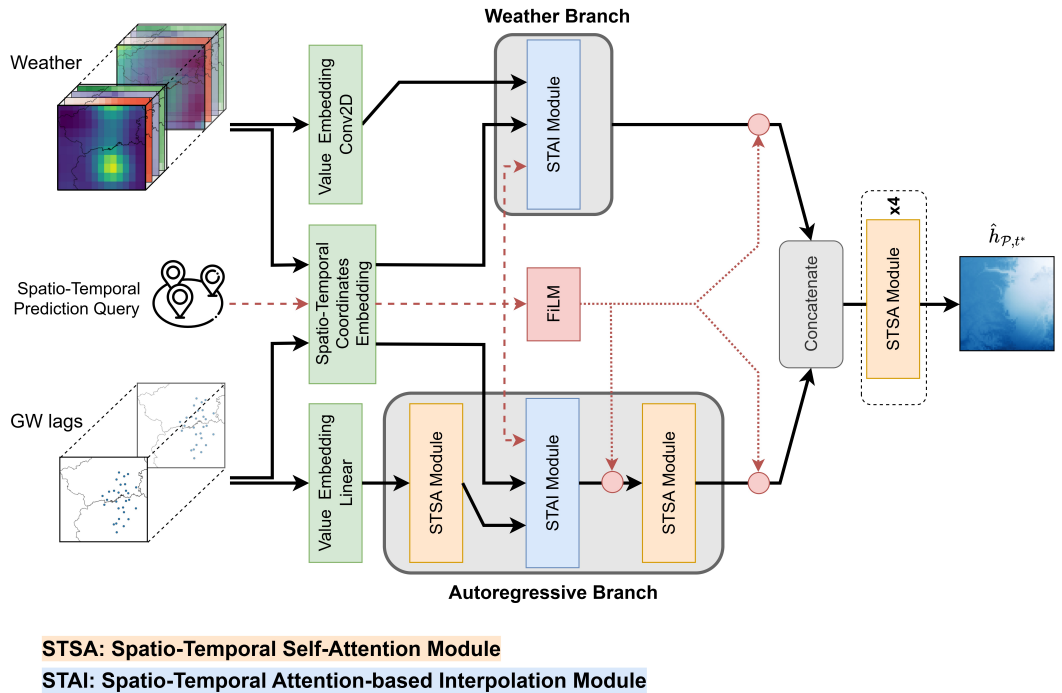


Figure 4: STAINet architecture.

To further condition the model on the spatio-temporal location of the prediction points, we adopted the Feature-wise Linear Modulation (FiLM) conditioning [37]. The FiLM layer performs a conditional feature normalization by scaling and shifting every feature channel. In particular, the scale and shift factors are computed by a linear layer from the conditioning information – in our case, the augmented spatio-temporal coordinates of the prediction points. This mechanism enables adaptation of neural representations to the conditioning information, facilitating the learning of complex context-dependent relations and improving the generalization ability of the model.

We named our pure deep learning model Spatio-Temporal Attention-based Interpolation neural

Network (STAINet), and its architecture is depicted in Figure 4. We decided to process the autoregressive component and the weather one, with two parallel branches. In particular, we designed an Autoregressive Branch that begins with one STSA module. During training, the MHA layer adopted in this first module employs dropout to randomly omit part of the input key-value pairs, thereby enhancing the model’s generalization capability and preventing it from focusing on specific input locations [3]. Subsequently, to extract the relevant information from the input points, an STAI module projects the hidden representation of the spatio-temporal value embedding (i.e., the output of the previous STSA module) onto the spatio-temporal prediction query, followed by an additional STSA module. The FiLM conditioning is adopted both after the STAI module and after the last STSA module to force the hidden representations to capture context-dependent relationships and facilitate the model in differentiating among prediction points.

This configuration was found to be the optimal choice for the Autoregressive Branch, balancing models’ complexity with the ability of learning complex dependencies from in situ spatially sparse measurements.

To handle the exogenous weather information, we defined the Weather Branch, which is made only of one STAI module, whose outputs are conditioned by the FiLM layer. The inclusion of STSA modules in this branch did not prove effective; on the contrary, it made the training process more difficult and reduced the models’ generalization capability. This behaviour is likely attributable to the use of the time-distributed convolutional embedding layer for constructing the ST-VEmb, which already encapsulates the relevant spatial information.

For the pure deep learning model, the two branches were concatenated, and the resulting hidden representation was passed through four stacked STSA modules. The output is then processed by a last linear layer that produces the predictions for all the desired points.

Due to differences in the time series across sensors, we adopted the Mean Absolute Percentage Error (MAPE) as the data loss term (\mathcal{L}_{data}) since it proved more effective than other non-relative loss functions. Furthermore, we introduced an orthogonality regularization term \mathcal{L}_{ortho} to enforce orthogonality on the weights of the embedding layers. This constraint encouraged the embeddings to capture non-redundant features [38, 39].

4.2 Physics-Guided Approach

Considering the PDE in Equation (4), applying the Euler integration method, we then expressed h at a time t^* (h_{t^*}) as a function of its Δt lag ($h_{t^*-\Delta t}$), as in Equation (7).

$$h_{t^*} = h_{t^*-\Delta t} + \Delta t \left[\frac{T}{S} \left(\frac{\partial^2 h}{\partial x^2} + \frac{\partial^2 h}{\partial y^2} \right) \right] \quad (7)$$

To simplify the notation, we defined the diffusion parameter $\mathcal{D} = \frac{T}{S}$ expressed in [L^2T^{-1}], and $\Delta_{GW_{t^*}} = \Delta t \left[\mathcal{D} \left(\frac{\partial^2 h}{\partial x^2} + \frac{\partial^2 h}{\partial y^2} \right) \right]$ expressed in [L]. We further add a residual (sink/source) term \mathcal{R}_{t^*} expressed in [L] related to all exogenous factors occurring in the interval Δt , which can be either anthropogenic (e.g., water abstraction for irrigation) or natural (e.g., rainfall or snowmelt recharge). We thus obtained Equation 8:

$$h_{t^*} = h_{t^*-1} + \Delta_{GW_{t^*}} + \mathcal{R}_{t^*} \quad (8)$$

Hereafter, we refer to h_{t^*-1} as the autoregressive component and to $\Delta_{GW_{t^*}}$ as the diffusion displacement component. In our setting, we considered Δt equal to one week.

4.2.1 Inductive Bias Strategy As an initial approach to incorporate physical knowledge into the deep learning model, we modified STAINet to explicitly output the three components defined earlier, computing the final output as the sum of these components. To this end, we developed the PSTAINet-IB (Physics-guided STAINet with Inductive Bias), which is depicted in Figure 6.

The initial part of the architecture follows the same structure as the STAINet; however, PSTAINet-IB does not concatenate the two branches. In particular, the \mathcal{R}_{t^*} and $h_{\mathcal{P},t^*-1}$ terms are estimated by two linear layers. Differently, since the diffusion component $\Delta_{GW_{t^*}}$ is more complex, we employed a more advanced neural structure for its estimation.

Firstly, the \mathcal{D} Block estimates the parameter \mathcal{D} , taking as input the spatial coordinates and elevation of the prediction points. It is implemented as an MLP comprising three linear layers (Figure 5a), followed by Instance Normalization and LeakyReLU activation. We designed the \mathcal{D} Block under the assumption that \mathcal{D} is a time-invariant property of the soil, and thus can be estimated based on spatial coordinates. Although simple in structure, this block provides hydrologically consistent estimations of \mathcal{D} while keeping the number of trainable parameters low. We then developed the Δ_{GW} module

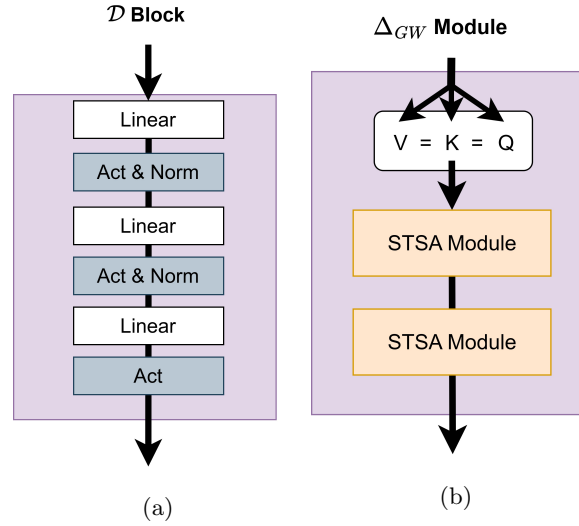
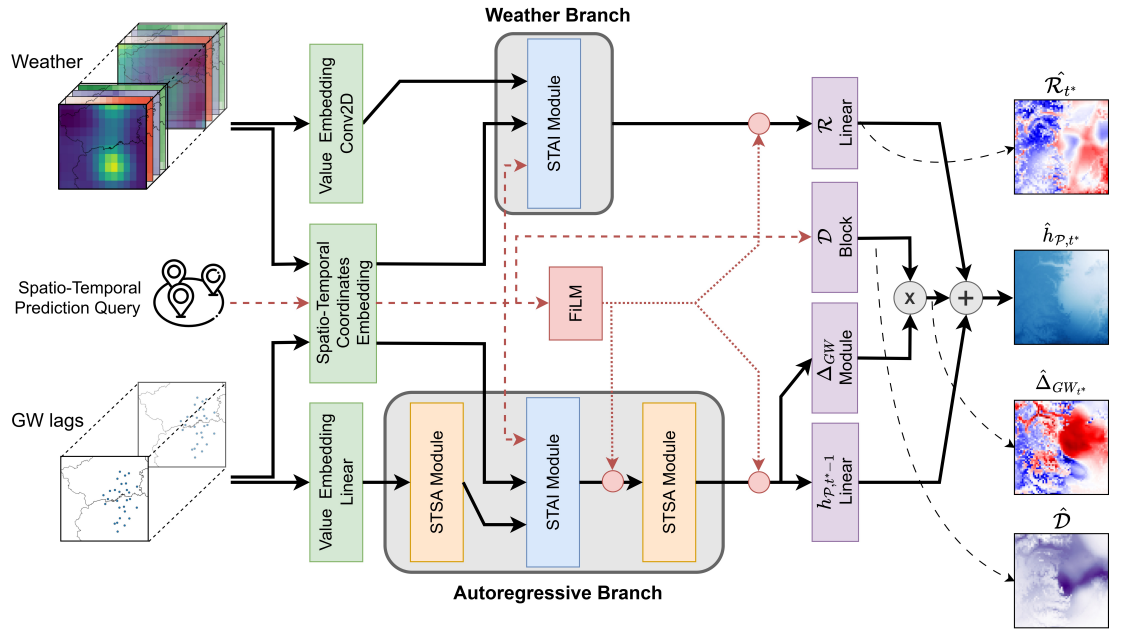


Figure 5: **a)** \mathcal{D} Module in which Act & Norm stand for activation and normalization respectively; **b)** Δ_{GW} Module.



STSA: Spatio-Temporal Self-Attention Module

STAI: Spatio-Temporal Attention-based Interpolation Module

Figure 6: PSTAINet-IB architecture.

(Figure 5b), consisting of a stack of two STSA modules, to estimate the divergence term $\frac{\partial^2 h}{\partial x^2} + \frac{\partial^2 h}{\partial y^2}$. In the Δ_{GW} module, we adopted STSA modules in place of MLP to enable the estimation of more complex relationships among prediction points. The diffusion component is then computed as the multiplication of the estimated \hat{D} and divergence term (Δt is omitted as we set it equal to one).

During the training of the model PSTAINet-IB, the three terms were not directly supervised; only their sum, corresponding to the final output of the model, was used in the calculation of the data loss function \mathcal{L}_{data} .

4.2.2 Learning Bias Strategy We then tested a second strategy consisting of adding learning biases to the PSTAINet-IB. Firstly, we supervised the estimated autoregressive component using the MAPE between \hat{h}_{p,t^*-1} and the true data h_{p,t^*-1} , to make the lag estimation coherent with the available data, we named this loss term \mathcal{L}_{coh} .

Subsequently, we computed the Mean Squared Error (MSE) of the residuals between the estimated diffusion displacement and its discretized version computed on the estimated lag – we named the

loss built on these residuals $\mathcal{L}_{\text{diff}}$. In detail, we applied the finite difference method with a central difference approximation [40] to compute the second-order spatial derivatives of $\hat{h}_{\mathcal{P},t^*-1}$. To compute this discretized approximation, a spatially dense estimated lag is needed, i.e., a gridded map. It is worth noting that this loss can be computed on arbitrary prediction points, named control points in the PINN literature, and does not require true data for supervision.

We further introduced some regularization terms on the ℓ^1 and ℓ^2 norms of the $\hat{\mathcal{R}}$ to constrain its mean value toward zero and mitigate high-magnitude responses, termed $\mathcal{L}_{\|\mathcal{R}\|_1}$ and $\mathcal{L}_{\|\mathcal{R}\|_2}$, respectively. We named the model with these learning biases PSTAINet-ILB (Physics-guided STAINet with Inductive and Learning Biases).

Finally, we leverage the domain knowledge of recharge zones, which are the zones where the groundwater body recharges due to precipitation and snowmelt. In our ROI, ARPA experts defined the recharge zones for the groundwater body in an area at the base of the mountain⁴. We considered a buffer of 0.05° and defined a loss term \mathcal{L}_{RCH} that penalizes positive values of \mathcal{R} outside the recharge zones. Formally, defining \mathcal{R}^+ as the positive value of \mathcal{R} , RCH as the set of points inside the recharge zones, and its complement RCH^c , $\mathcal{L}_{RCH} = \frac{1}{\sum \mathbf{1}_{RCH^c}(\mathcal{R}^+)} \sum \mathbf{1}_{RCH^c}(\mathcal{R}^+) \mathcal{R}$. We named the model trained with this further regularization PSTAINet-ILRB (Physics-guided STAINet with Inductive, Learning, and Recharge zone Biases).

The final loss is then the summation of all terms previously described (if adopted by the considered model), as in Equation (9):

$$\begin{aligned} \mathcal{L} = & \mathcal{L}_{\text{data}} + \alpha_{\text{ortho}} \mathcal{L}_{\text{ortho}} + \alpha_{\text{coh}} \mathcal{L}_{\text{coh}} + \alpha_{\text{diff}} \mathcal{L}_{\text{diff}} \\ & + \alpha_{\|\mathcal{R}\|_1} \mathcal{L}_{\|\mathcal{R}\|_1} + \alpha_{\|\mathcal{R}\|_2} \mathcal{L}_{\|\mathcal{R}\|_2} + \alpha_{RCH} \mathcal{L}_{RCH} \end{aligned} \quad (9)$$

Table 1: Hyperparameters.

Model	α_{ortho}	α_{coh}	α_{diff}	$\alpha_{\ \mathcal{R}\ _1}$	$\alpha_{\ \mathcal{R}\ _2}$	α_{RCH}
STAINet	10^{-3}	-	-	-	-	-
PSTAINet-IB	10^{-3}	-	-	-	-	-
PSTAINet-ILB	10^{-3}	1	$2.5 \cdot 10^{-2}$	$5 \cdot 10^{-4}$	10^{-4}	-
PSTAINet-ILRB	10^{-3}	1	$2.5 \cdot 10^{-2}$	$5 \cdot 10^{-4}$	10^{-4}	$5 \cdot 10^{-4}$

5 Experiments

We supplied the models with information from the four weeks preceding each prediction (lags $\mathcal{T} = 4$), as this configuration yielded the best performance while avoiding an excessive amount of uninformative data. For all four models STAINet, PSTAINet-IB, PSTAINet-ILB, and PSTAINet-ILRB, we set the embedding dimension equal to 32 and the number of heads for each MHA layer to 8. Under these settings, STAINet contained a total of 62081 trainable parameters, while PSTAINet-IB, PSTAINet-ILB, and PSTAINet-ILRB each comprise 49666 trainable parameters. All models were trained using AdamW optimizer [41] with a learning rate of $2.5 \cdot 10^{-4}$ decreased to 10^{-4} at epoch 400, and a weight decay equal to $2.5 \cdot 10^{-3}$. The total number of epochs to achieve a relevant optimum was found to be 1000 for STAINet, 850 for PSTAINet-IB and PSTAINet-ILRB, while 600 for PSTAINet-ILB. The dropout rate in the initial Spatio-Temporal Self-Attention block of the Autoregressive Module was set to 0.15 for all configurations. The weights assigned to the individual loss components are reported in Table 1. All the mentioned hyperparameters were found by manual grid search.

We compared the model performances considering the median over all sensors of NBIAS, RMSE, MAPE, Nash–Sutcliffe Efficiency (NSE), and Kling–Gupta Efficiency (KGE), described in Equations 10, 11, 12, 13, and 14, computed between true data h and the prediction \hat{h} for every sensor over the test set of length $N = 104$ (weeks), and with σ and μ representing the variance and mean respectively. To evaluate further the model’s generalization ability, we tested the models feeding both the true lags as input and in a rollout setting using the predictions at the previous time step as the lagged input for the whole test, i.e. $\hat{h}_{\mathcal{P},t^*} = \hat{f}_\theta(H_{\mathcal{P},t^*-1}, \mathbf{V}_{t^*})$ and $\hat{h}_{\mathcal{P},t^*} = \hat{f}_\theta(\hat{H}_{\mathcal{P},t^*-1}, \mathbf{V}_{t^*})$, respectively. Thus, in the last case, models see only true groundwater level data at the beginning of the test set (2022-01-01), and then they iterate their predictions to produce the whole test set’s predictions.

Since the model can generate predictions at an arbitrary number of points, it enables the production of groundwater level maps at any desired spatial resolution (as shown in the output of Figure 4).

⁴Available here: <https://shorturl.at/qTheu>.

Therefore, we produced dense prediction maps at a spatial resolution of 1.5km per pixel. Specifically, prediction points were placed approximately every 1.5km, and all points were jointly predicted by the models. This allowed us to assess both the coherence of the predictions and the behaviour of the predicted equation components throughout the ROI area⁵.

Finally, the best-performing model was used to predict the full time series (starting from 2001-01-01) for all sensors, assessing its capability to replicate the observed data. In this last case, we produced rollout predictions with a forecast horizon of 26 time steps, i.e., feeding true data every 26 time steps, and iterating the predictions in between.

$$RMSE = \sqrt{\frac{1}{N} \sum_i^N (\hat{h}_i - h_i)^2} \quad (10)$$

$$NBIAS = \frac{\frac{1}{N} \sum_i^N (\hat{h}_i - h_i)}{h_{max} - h_{min}} \quad (11)$$

$$MAPE = 100 \frac{1}{N} \sum_i^N \frac{|\hat{h}_i - h_i|}{h_i} \quad (12)$$

$$NSE = 1 - \frac{\sum_i^N (\hat{h}_i - h_i)^2}{\sum_i^N (h_i - \bar{h})^2} \quad (13)$$

$$KGE = 1 - \sqrt{(\rho - 1)^2 + (\alpha - 1)^2 + (\beta - 1)^2} \quad (14)$$

$$\alpha = \frac{\sigma_{\hat{h}}}{\sigma_h}; \beta = \frac{\mu_{\hat{h}}}{\mu_h}$$

6 Results

Table 2 reports the median evaluation metrics over all sensors computed on models' predictions feeding real data and in the rollout setting. In both cases, the best-performing model was PSTAINet-ILB. In general, all models with the physics prior performed better than the pure deep learning approach (STAINet), suggesting that both the inductive bias and the learning bias strategies provided useful information to the models. On most of the metrics, PSTAINet-ILRB performed better than the PSTAINet-IB, but worse than the PSTAINet-ILB. This might suggest that the recharge zones prior was too restrictive, limiting the model's representation ability. The metrics computed on every sensor and every model in the rollout setting are reported in Section B, specifically in Table 5, Table 6, Table 7, Table 8.

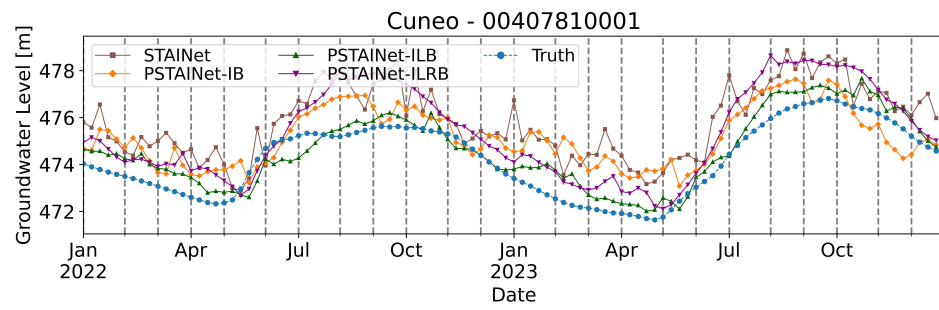
Figure 7 depicts the predictions on the test set, feeding true data and iterating the predictions (rollout setting), respectively, for the sensors in Cuneo, Racconigi, Scalenghe, and Vottignasco. In Section B, we reported the predictions over the test set for all the sensors, in the rollout setting (Figure 21).

From Figure 7, the good generalization ability of the PSTAINet-ILB model is visible, especially in contexts of unprecedented drop, like in the summers of 2022 and 2023. PSTAINet-ILRB also predicted the decreases in the water level among all sensors accurately, but in some cases (like in Scalenghe, Figure 7f) the drops were not accurately predicted, and in other cases (like Racconigi, Figure 7d) a premature recharge was predicted.

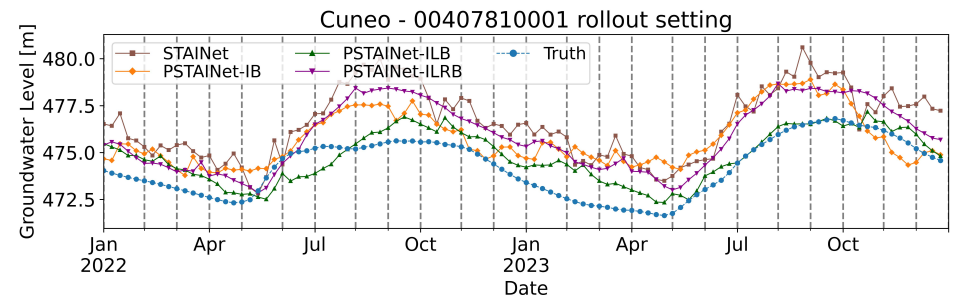
Even if differences between feeding true data and the rollout setting are visible (Tables 2 and from Figure 7, the PSTAINet-ILB model maintained almost the same performance. This further demonstrates the good generalization ability of the PSTAINet-ILB model.

Figure 8 shows the map predictions at a resolution of 1.5km/pixel for the week starting on 2022-07-17. All models predicted a map in line with the expert domain expectations (i.e., with higher groundwater levels in the mountain region). However, the PSTAINet-ILB and PSTAINet-ILRB predictions appear to be less definite on the north-west mountains, but they better identified the rivers and valleys in the southeastern part. Notwithstanding, a formal evaluation of these results is difficult because of the lack of true measured data all over the ROI, especially in the mountains – a universal problem in hydrology.

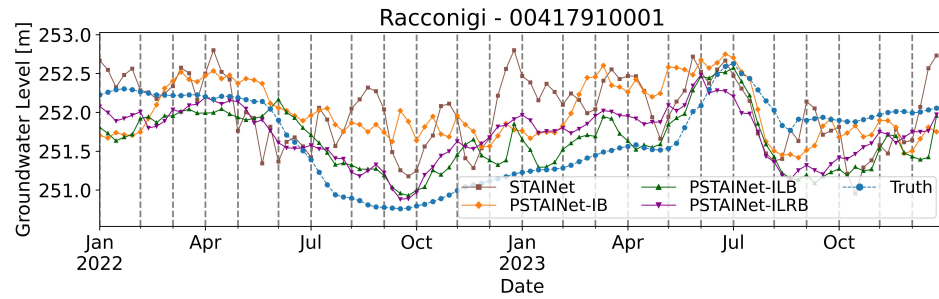
⁵The code is available here <https://github.com/Matteo-Salis/physics-guided-gwl> along with GIFs representing the prediction maps evolution through time



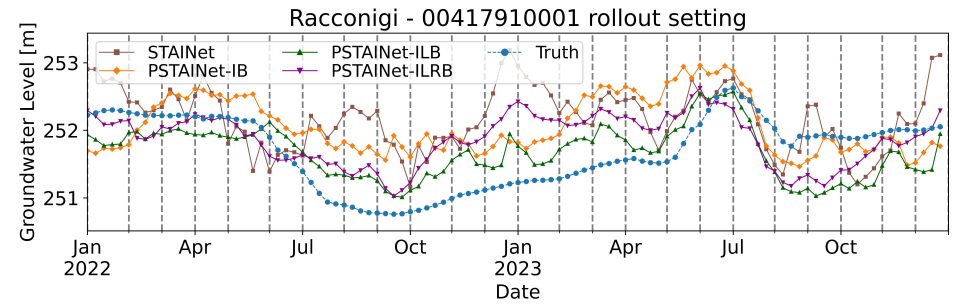
(a)



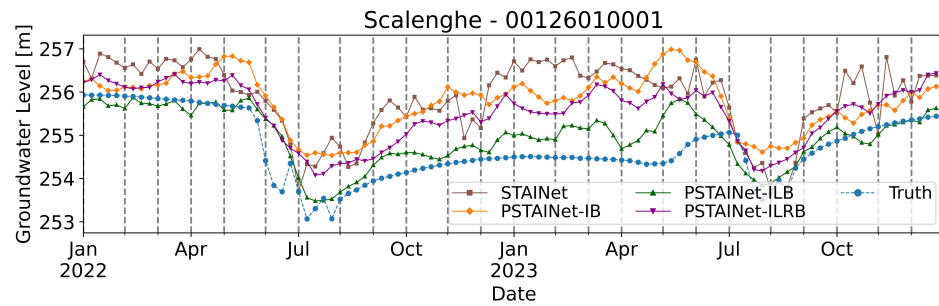
(b)



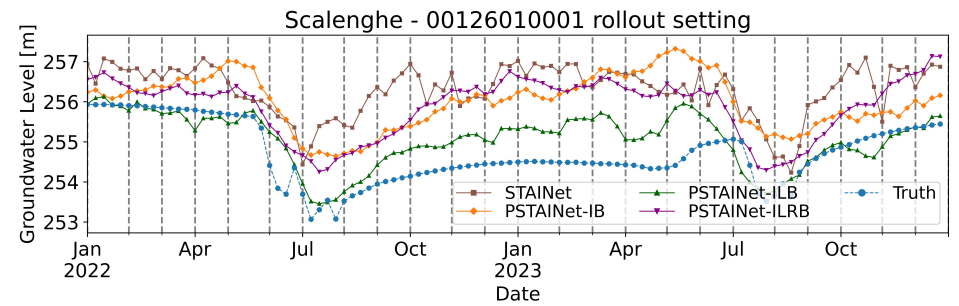
(c)



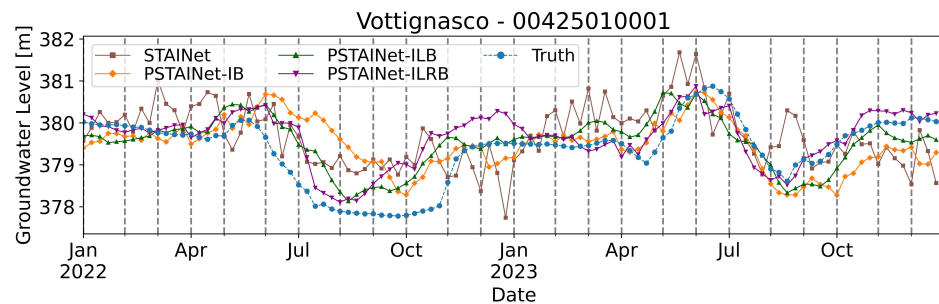
(d)



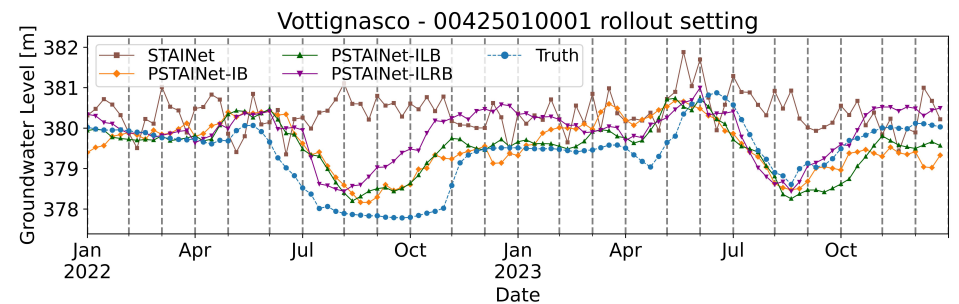
(e)



(f)



(g)



(h)

Figure 7: STAINet, PSTAINet-IB, PSTAINet-ILB, and PSTAINet-ILRB predictions on the test set feeding true data in **a), c), e), g)** and in the rollout setting **b), d), f), h)** in Cuneo, Racconigi, Scalenghe, and Vottignasco.

Table 2: Median performance metrics on Test set feeding true data (True Data) and in the rollout setting (Rollout).

	STAINet		PSTAINet-IB		PSTAINet-ILB		PSTAINet-ILRB	
	True Data	Rollout	True Data	Rollout	True Data	Rollout	True Data	Rollout
NBIAS	0.1042	0.1713	0.0594	0.0862	-0.0093	0.0124	0.0177	0.0685
RMSE [m]	0.8351	1.0292	0.6296	0.7336	0.5058	0.5851	0.6521	0.6783
MAPE [%]	0.2834	0.2868	0.2319	0.2606	0.1479	0.1604	0.1900	0.1953
NSE	0.5612	0.2884	0.7059	0.6269	0.8025	0.7876	0.7986	0.7024
KGE	0.2583	0.2236	0.4253	0.5196	0.5917	0.5800	0.5018	0.4074

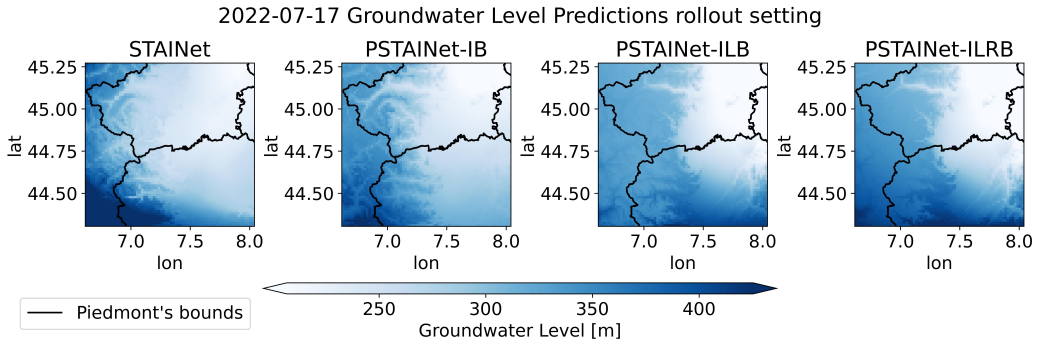


Figure 8: STAINet, PSTAINet-IB, PSTAINet-ILB, and PSTAINet-ILRB groundwater level prediction maps at 1.5km/pixel for 2022-07-17.

7 Discussion

An extensive comparison with existing studies is challenging due to the specificity of our application and the scarcity of research employing physics-guided strategies on real groundwater level measurement data.

However, a reference work exists [42], in which authors trained sensor-specific pure data-driven neural networks on a subset of groundwater sensors considered in our study. Although our proposed models are not sensor-specific, we achieved comparable performance, considering the PSTAINet-ILB median NBIAS -0.01 versus -0.05 of [42], NSE 0.80 versus 0.90, and KGE 0.59 versus 0.43. Our performance are consistent also with those reported in other studies that adopt data driven models to estimate groundwater levels in different geographical regions, such as [43] in Yangpyeong riverside area (South Korea) and [44] in the Upper Rhine Graben area (central Europe), which achieved NSE values of nearly 0.8 and 0.5, respectively.

In the following, a more detailed analysis of the results of our proposed models is presented.

7.1 Loss Analyses

Figures 9a and 9b, which report the values of \mathcal{L}_{data} on the training and test sets, indicate that PSTAINet-ILB and PSTAINet-ILRB exhibit superior generalization ability. Specifically, although both models obtained higher training \mathcal{L}_{data} values, they achieved lower test errors, demonstrating better out-of-sample performance. Furthermore, even if PSTAINet-ILB has been trained for fewer epochs (600) it achieved the best performance, further proving the utility of the adoption of both inductive and learning bias strategies. Nevertheless, the introduction of learning biases substantially increased the time required for completing a training epoch, especially due to gradient computations, which was on average 4.616s for STAINet, 4.157s for PSTAINet-IB, 18.286s for PSTAINet-ILB, and 18.697s for PSTAINet-ILRB.

Figures 9c, 9d, and 9e report the values of \mathcal{L}_{coh} , \mathcal{L}_{diff} , and \mathcal{L}_{RCH} on the training set, respectively. Both \mathcal{L}_{coh} and \mathcal{L}_{RCH} exhibit a monotonic decrease over the course of training, whereas \mathcal{L}_{diff} shows an initial decline followed by a subsequent rebound for both models. This behaviour may stem from interactions or conflicts among the different loss terms, but it may also be attributed to noise, given the very small magnitudes reached by \mathcal{L}_{diff} (see the y-axis in Figure 9d). A more in-depth analysis of these loss dynamics is left for future work.

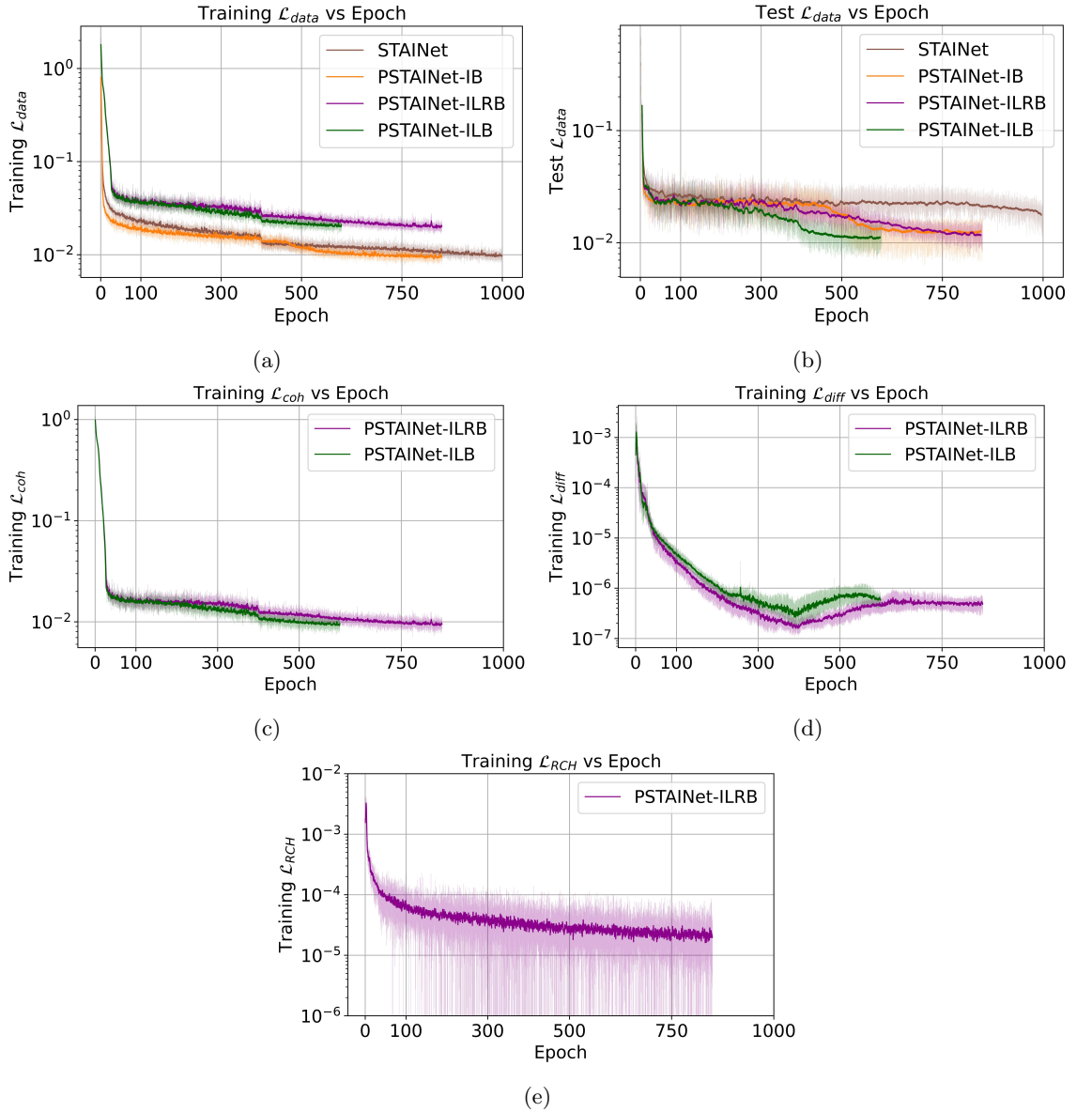


Figure 9: Loss plots **a)** training \mathcal{L}_{data} , **b)** test \mathcal{L}_{data} , **c)** training \mathcal{L}_{coh} , **d)** training \mathcal{L}_{diff} , **e)** training \mathcal{L}_{RCH} .

7.2 Error Analyses

7.2.1 Missing Data Analysis To analyze the missing data effect on model performance, we studied the correlation between MAPE and missing values. Figure 10 depicts the scatterplots and the Pearson correlation between MAPE and missing values for all sensors in the rollout setting. A slight positive correlation is observed for all the models, from 0.1 for the PSTAINet-ILRB to 0.24 for the PSTAINet-ILB. The points with the highest MAPE for the STAINet, PSTAINet-IB, and PSTAINet-ILRB correspond to the Buriasco and Orbassano sensors, which appear somewhat isolated in the scatterplot. The high MAPEs may be related to the large amount of missing data in recent years and to the pronounced decline observed in their measurements.

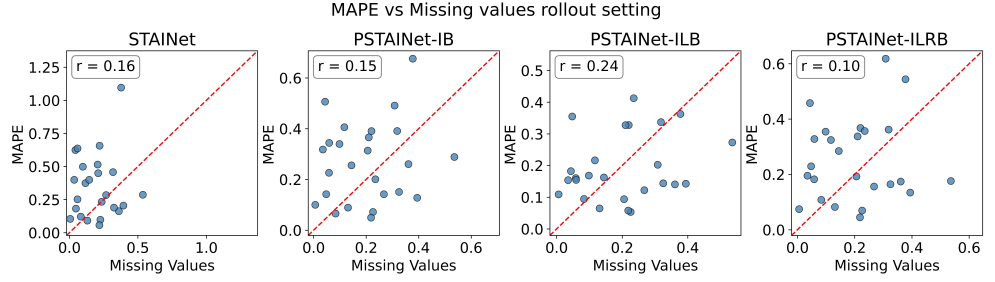


Figure 10: Correlation plots between MAPE and missing values percentage for STAINet, PSTAINet-IB, PSTAINet-ILB, and PSTAINet-ILRB; in all plots, the red line is the bisector and r is Pearson’s correlation coefficient.

7.2.2 Temporal Error Analysis In Figure 11 we reported the MAPE averaged over all sensors for each date of the test set, along with the corresponding standard deviation. PSTAINet-ILB showed the lowest mean MAPE, with slightly higher errors in summer 2022 and summer 2023 – the former affected by a severe drought. STAINet, and PSTAINet-ILRB produced bigger errors in summer and autumn 2022 related to the drop, not well predicted, in groundwater levels in many locations (see Carmagnola in Figure 21h, Cavour in Figure 21k, Fossano in Figures 21m and 21n, and Tarantasca in Figure 21u). This behaviour is also observed, though less accentuated, for the PSTAINet-IB model, which produced slightly larger errors also during spring 2023. Nevertheless, given the limited length of the test set, it is difficult to state seasonal error patterns for the models. It would be necessary to have more observations from additional years as a test set – a condition that will be met in the near future, once data from the 2024 and 2025 field measurement campaigns become available.

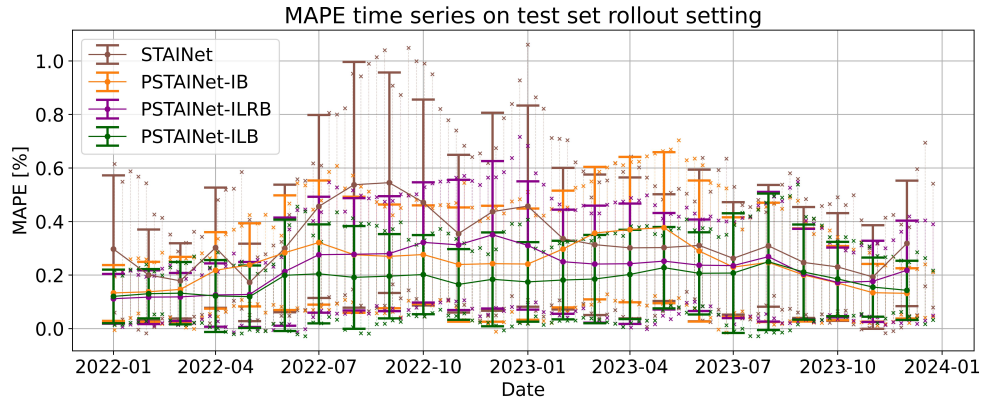


Figure 11: Average MAPE over all sensors in the rollout setting on the test set. Vertical dashed lines represent the MAPE standard deviation for each week, while vertical dense bold lines represent the corresponding monthly averages and standard deviations.

7.2.3 Trend & Seasonality Analysis We also investigated the association between the trend and seasonality of the groundwater level time series and the error, specifically with MAPE and KGE. In more detail, we decompose each time series with a Seasonal and Trend decomposition using LOESS⁶ (STL) [45] assuming each time series Y as a summation of three terms, namely a trend component T , a seasonal component S , and a residual component R , in other words $Y = T + S + R$. Firstly, the trend component T is estimated using LOESS to capture the overall direction of the series by smoothing short-term fluctuations. Then, on the residual between T and the original Y , the seasonal term S is estimated to extract repeated patterns occurring at the yearly scale. Lastly, the residual component R is determined as the remaining fluctuations not captured by the other two terms⁷.

We then adopted metrics to quantify the strength of the seasonal and trend components, specifically the Trend Strength \mathcal{S}_T (Equation 15) and the Seasonal Strength \mathcal{S}_S (Equation 16) [46]:

$$\mathcal{S}_T = \max\left(0, 1 - \frac{\text{Var}(R)}{\text{Var}(T + R)}\right) \quad (15)$$

⁶LOESS stands for LOcally Estimated Scatterplot Smoothing, which is a non-parametric local non-linear regression statistical method.

⁷For more technical details, please refer to [45]

$$\mathcal{S}_S = \max\left(0, 1 - \frac{\text{Var}(R)}{\text{Var}(S + R)}\right) \quad (16)$$

Figures 12 and 13 report the scatterplots and the Pearson correlation between MAPE versus \mathcal{S}_T , and KGE versus \mathcal{S}_T , respectively. For all models, a fairly strong positive correlation (ranging from 0.39 to 0.52) is present between MAPE and \mathcal{S}_T while a negative one with KGE (ranging from -0.52 to -0.25), stating that the stronger the trend of each time series, the lower the performances are. Indeed, a stronger trend component might indicate a nonstationary time series, which is more difficult to model, especially if the nonstationarity is caused by external factors (e.g., drought and climate change).

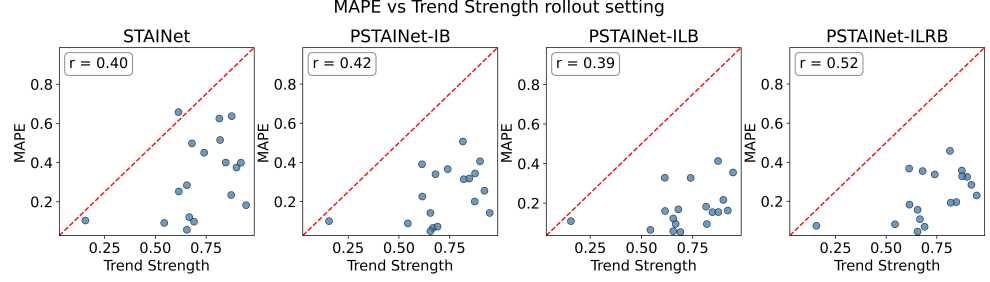


Figure 12: Correlation plots between MAPE and Trend Strength \mathcal{S}_T for STAINet, PSTAINet-IB, PSTAINet-ILB, and PSTAINet-ILRB; in all plots, the red line is the bisector and r is Pearson's correlation coefficient.

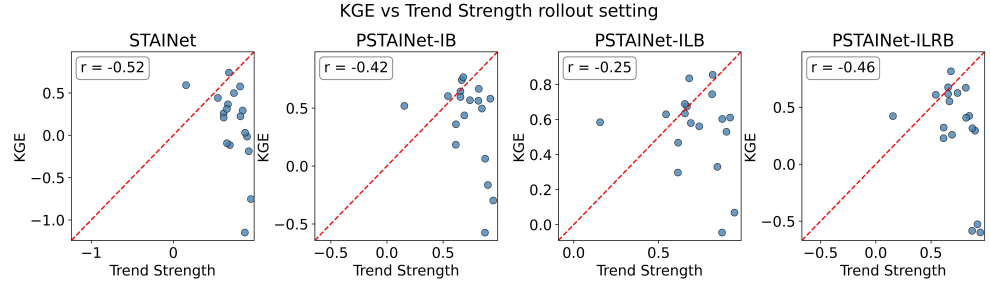


Figure 13: Correlation plots between KGE and Trend Strength \mathcal{S}_T for STAINet, PSTAINet-IB, PSTAINet-ILB, and PSTAINet-ILRB; in all plots, the red line is the bisector and r is Pearson's correlation coefficient.

Conversely, as Figures 14 and 15 show, a positive correlation appeared between KGE and \mathcal{S}_S (ranging from 0.43 to 0.55), while a low, and partially negative, one with MAPE (ranging from -0.12 to 0.08). This means that models do not show any definite relation between the absolute percentage errors and stronger seasonal patterns. However, stronger seasonalities ease the prediction of the dynamical pattern of the time series (higher KGE) – an expected association given that a stronger seasonality means a clearer repeated pattern through time.

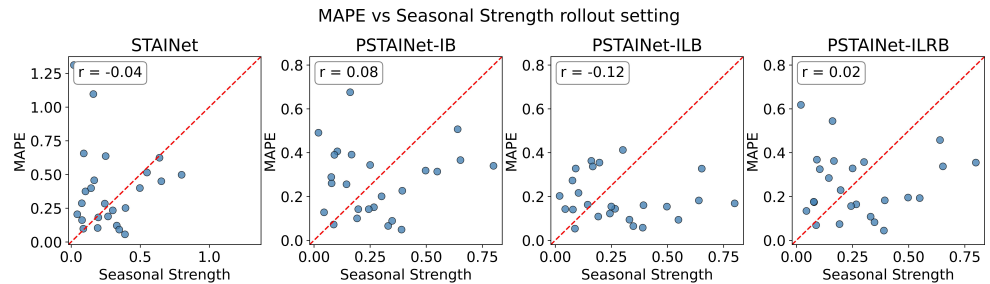


Figure 14: Correlation plots between MAPE and Seasonal Strength \mathcal{S}_S for STAINet, PSTAINet-IB, PSTAINet-ILB, and PSTAINet-ILRB; in all plots, the red line is the bisector and r is Pearson's correlation coefficient.

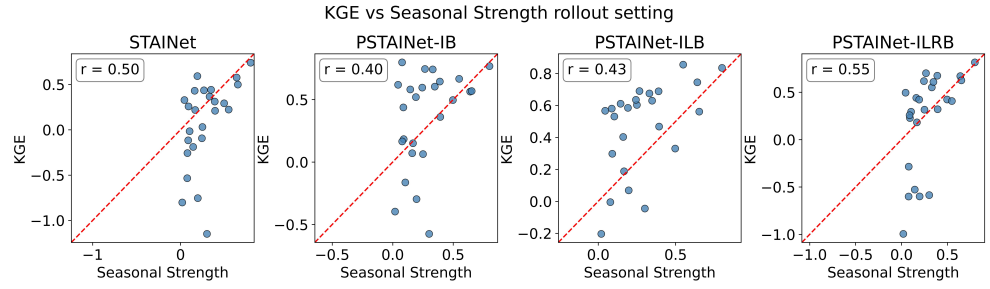


Figure 15: Correlation plots between KGE and Seasonal Strength \mathcal{S}_S for STAINet, PSTAINet-IB, PSTAINet-ILB, and PSTAINet-ILRB; in all plots, the red line is the bisector and r is Pearson's correlation coefficient.

7.2.4 Spatial Error Analysis Figure 16 and Figure 17 report the NBIAS and MAPE for all sensors in the rollout setting, respectively. Overall, the models tended to overestimate groundwater levels, as indicated also by the positive median NBIAS values reported in Table 2. Among all models, the PSTAINet-ILB exhibited the smallest NBIAS, showing a more balanced spatial pattern – with slight underestimations in the northern sensors and overestimations in the southern ones (Figure 16). The

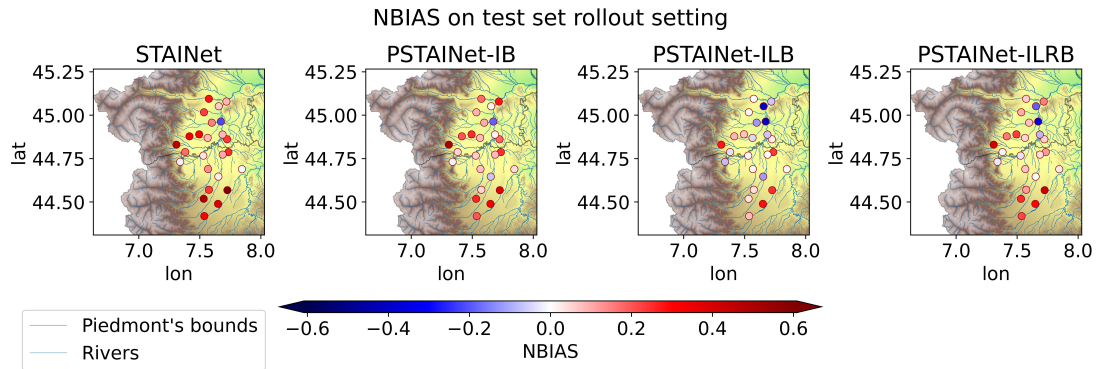


Figure 16: NBIAS for all sensors in the rollout setting on the test set.

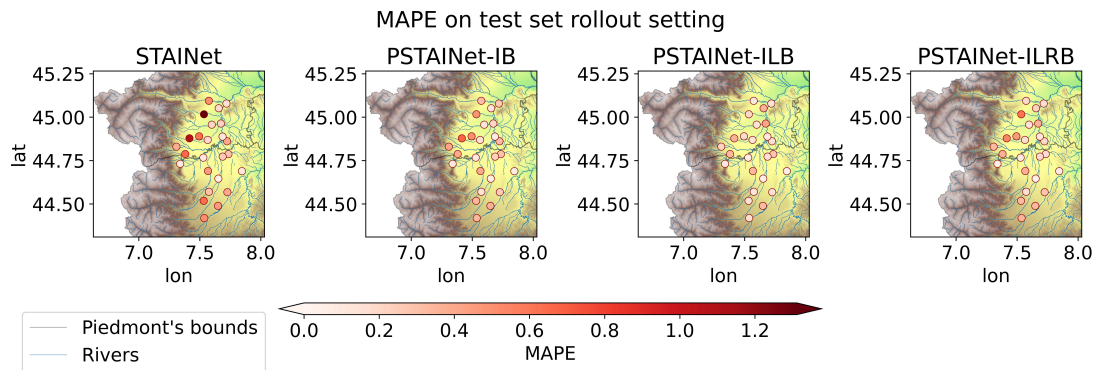


Figure 17: MAPE for all sensors in the rollout setting on the test set.

sensor located in La Loggia represented a challenging case for all models, which was underestimated by all of them (as shown also in Figure 21o). This could be due to the high number of missing data in the last year, but also because this sensor is among the few that did not exhibit a pronounced decreasing trend in recent years (see Figure 20 and in particular Figure 20o) – most likely as a result of its proximity to the Po River.

Concerning the spatial distribution of the MAPE in Figure 17, a mild tendency can be observed for higher MAPE values in the north-western and south-western sensors across all models (as for the NBIAS) apart from the PSTAINet-ILB, which displays a more even spatial pattern.

7.3 Predicted Equation Components

Apart from the better performance achieved, the proposed physics-guided models also provided an estimation of the terms of Equation (8). To assess the physical plausibility of the predictions, we analyzed the map predictions of the equation components, in particular, in the rollout setting.

Figures 18a, 18b, and 18c show the predicted PDE component on weeks starting on 2022-07-17, 2022-11-23, and 2023-03-12 respectively. PSTAINet-IB predicted a general displacement of groundwater from the mountains to the plain. However, the very high absolute value of $\hat{\Delta}_{GW_{t^*}}$ and $\hat{\mathcal{R}}_{t^*}$ undermined their physics soundness.

Differently, both PSTAINet-ILB and PSTAINet-ILRB provided insightful predictions also from the hydrological point of view. In particular, concerning the diffusion component $\hat{\Delta}_{GW_{t^*}}$, PSTAINet-ILB predicted in recharge periods (e.g., 2022-11-13 and 2023-03-12 in Figures 18b, and 18c respectively) a more pronounced groundwater discharge from mountains, while in dryer seasons, given the lower water content and precipitation, the discharge is limited, with water being more retained in the valleys and beneath the mountains. In contrast, the PSTAINet-ILRB model predicted a diffusion dynamic that remained more stable across different periods. Specifically, it captured a general outflow from the valleys toward the plain.

The two learning biased models learnt different physics relationships, and even though both appeared sensible, a rigorous evaluation of these processes is difficult, given the scarce knowledge of groundwater processes under mountains.

Looking at the sink/source predicted component $\hat{\mathcal{R}}_{t^*}$, the PSTAINet-ILB model detected a more pronounced and extended recharge areas during recharging seasons (Figures 18b, and 18c), while a more sparse pattern with alternated recharge and loss zones in dry seasons (Figure 18a) – probably because of more abstractions or higher temperatures in summer. Concerning the $\hat{\mathcal{R}}_{t^*}$ predictions made by PSTAINet-ILRB, the recharge zone regularization effect is clearly visible, limiting positive values of $\hat{\mathcal{R}}_{t^*}$ only into the delimited recharge zones (in green in Figures 18a, 18b, and 18c). Although this constraint is hydrologically reasonable, it may have been too restrictive in our case, where the shallow groundwater body is strongly influenced by surface forcing, both human and natural.

Finally, regarding the values of the predicted term $\hat{\mathcal{D}}$, all models produced plausible values. However, PSTAINet-ILB and PSTAINet-ILRB reported a more sensible spatial pattern with higher values in the valley that gradually attenuated through the plain.

In conclusion, the predicted equation component analysis suggests that the absence of supervision on the equation components may be problematic. Introducing regularization terms on $\hat{\Delta}_{GW_{t^*}}$ and $\hat{\mathcal{R}}_{t^*}$ enabled the models to generate results that are more in line with physics principles.

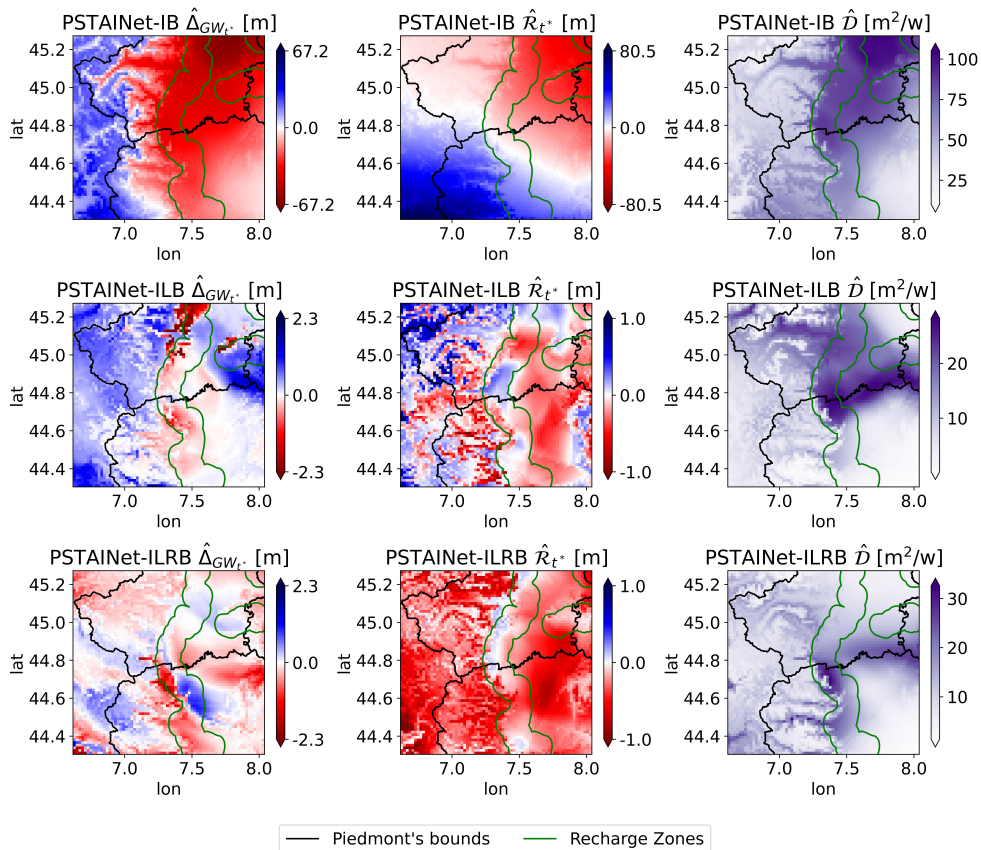
7.4 Time Series Reconstruction

We further evaluated the general ability of PSTAINet-ILB in reproducing the full available time series. Using PSTAINet-ILB, we predicted all the time series within a rollout setting with a forecast horizon of 26 weeks (i.e., 6 months). This is in line with the real situation in our case study, in which the ARPA releases groundwater level data on a semester basis. Table 3 reports the median evaluation metrics of the PSTAINet-ILB over all sensors, and Figure 19 depicts the predicted time series for Cuneo, Racconigi, Scalenghe, and Vottignasco. In Section C, we reported the metrics (Table 9) and the predicted time series (Figure 22) for all sensors separately. The model demonstrated strong capability in reconstructing the full time series, even during intervals with missing data, accurately reproducing seasonal dynamics as well as short-term fluctuations.

Table 3: PSTAINet-ILB time series reconstruction median Metrics, in the rollout setting with a 26 time step forecast horizon.

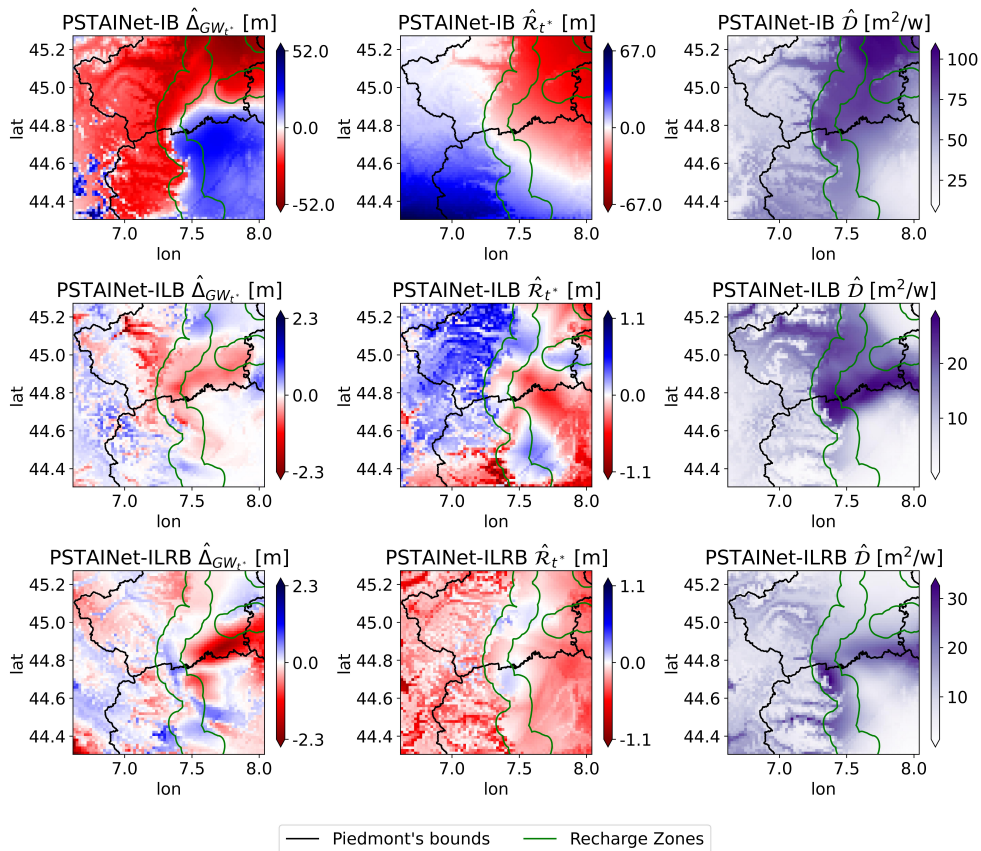
	NBIAS	RMSE [m]	MAPE [%]	NSE	KGE
PSTAINet-ILB	-0.0278	0.4490	0.1404	0.6314	0.7547

2022-07-17 Predicted Equation Components



(a)

2022-11-13 Predicted Equation Components



(b)

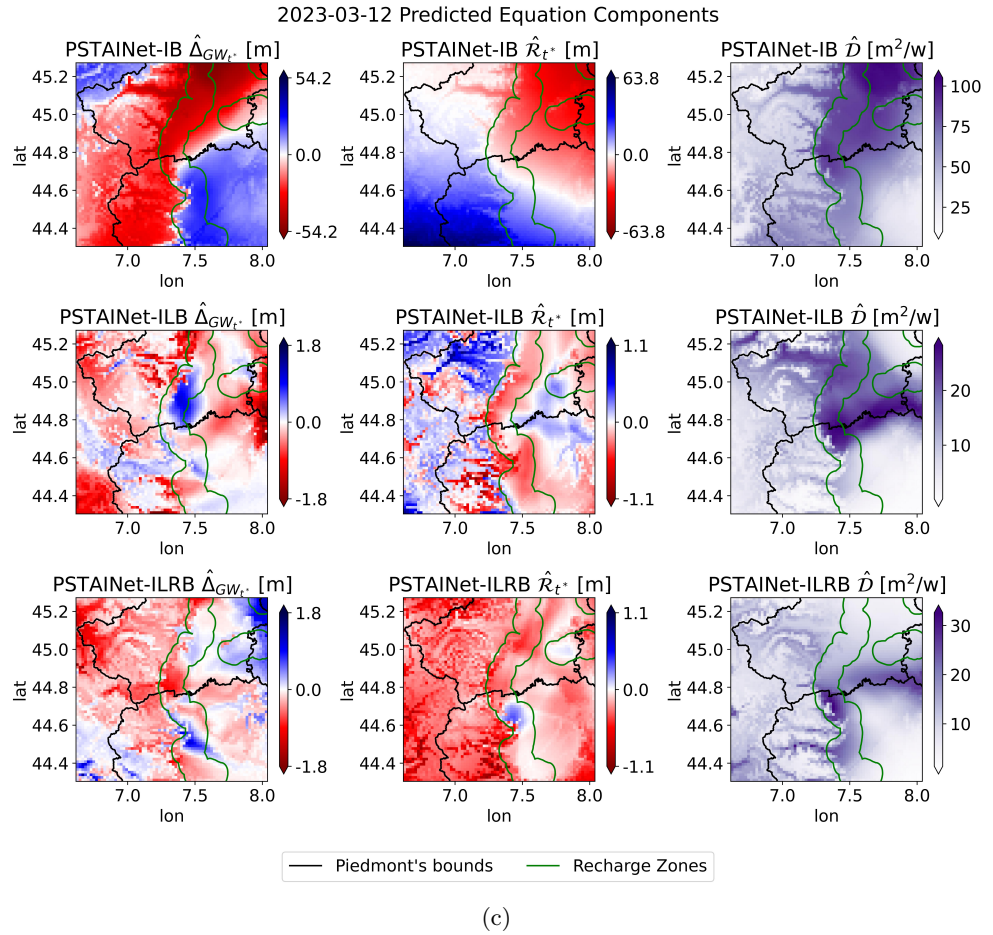
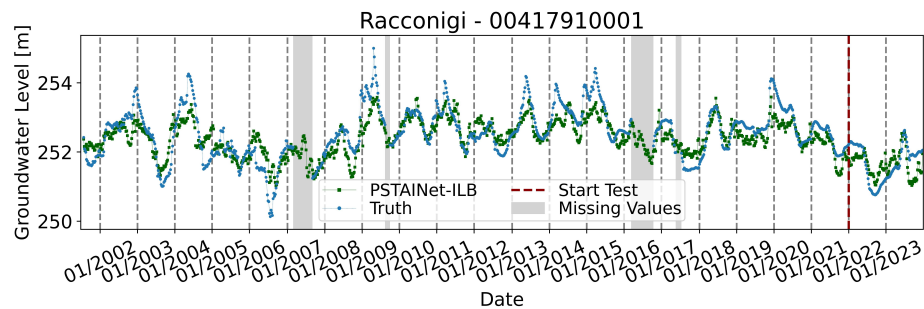
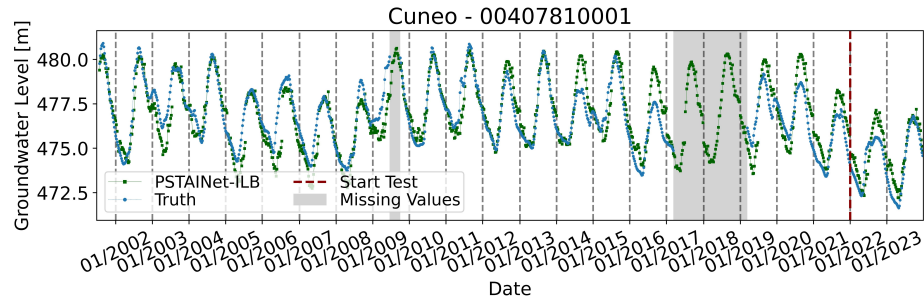


Figure 18: Predicted PDE components by PSTAINet-IB, PSTAINet-ILB, and PSTAINet-ILRB for the weeks starting on 2022-07-17 (a), 2022-11-13 (b) and 2023-03-12 (c). The first column reports $\hat{\Delta}_{GW_{t^*}}$, the second \hat{R}_{t^*} , and the last \hat{D} . Green lines identify the recharge zones. For $\hat{\Delta}_{GW_{t^*}}$, a blue pixel means inflow while a red one means outflow; for \hat{R}_{t^*} , a blue pixel means recharge while red represents a loss.



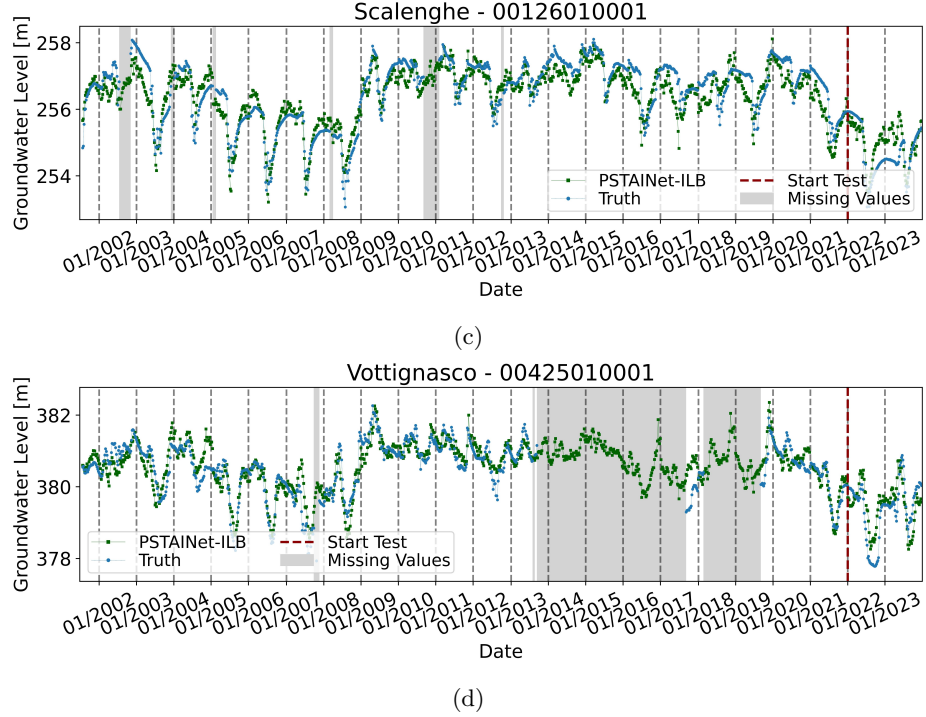


Figure 19: PSTAINet-ILB time series reconstruction in the rollout setting with a 26 time step forecast horizon for **a)** Cuneo, **b)** Racconigi, **c)** Scalenghe, and **d)** Vottignasco.

8 Conclusion

In this work, we aimed to develop deep learning models capable of generating predictions at any desired location within the ROI by leveraging spatially sparse in situ measurements (piezometers) together with spatially distributed meteorological data (weather video). Moreover, we investigated different bias strategies, namely inductive and learning biases, to incorporate physical knowledge derived from the groundwater flow equation into the models.

To this end, we first developed a purely deep learning model, STAINet, based on the Multi-Head Attention mechanism. We then proposed a restructured variant, PSTAINet-IB, using inductive bias by explicitly predicting the autoregressive ($h_{\mathcal{P}, t^* - 1}$), diffusion ($\Delta_{GW_{t^*}}$), and sink/source (\mathcal{R}_{t^*}) components of the governing equation. Furthermore, we derived the PSTAINet-ILB model by introducing regularization terms into the loss function to explicitly supervise these components (learning bias), and the PSTAINet-ILRB model by further integrating prior information on recharge zones. The PSTAINet-ILB model, trained adopting both inductive and learning bias strategies, achieved the best overall performance, accurately fitting the data while producing physically consistent equation components, thus enhancing model trustworthiness. Although PSTAINet-ILRB also performed well, it achieved slightly lower metrics, probably because of the too restrictive and uncertain nature of the recharge zone prior.

The predicted diffusion and sink/source components provide meaningful insights for assessing the physical soundness of the model and offer valuable information on groundwater dynamics in regions lacking piezometer coverage. In particular, while PSTAINet-IB produced implausible $\hat{\Delta}_{GW_{t^*}}$ and $\hat{\mathcal{R}}_{t^*}$ predictions, both PSTAINet-ILB and PSTAINet-ILRB produced physically consistent predictions, with PSTAINet-ILB especially capturing dynamics evolving accordingly to the recharge seasons.

The PSTAINet-ILB model demonstrated similar performance whether leveraging true data as lag inputs or iterating its own predictions over the entire test set (years 2022–2023), thus enabling long-term forecasts all over the ROI. This was further confirmed in the time series reconstruction task, where the complete series for all sensors were predicted using a six-month forecast horizon. In this task as well, the PSTAINet-ILB model achieved remarkable results – particularly given the challenges posed by missing data.

In conclusion, the adoption of inductive and learning biases has led to improved performance and enhanced the interpretability of deep learning models, despite several limitations remaining. With respect to the inductive bias, a limitation is the requirement of a closed-form equation that has to be explicitly hard-coded into the model – a condition that cannot always be satisfied in practice, especially in cases of partial or incomplete knowledge. Differently, under the learning-bias strategy,

the governing equation constraint must be formulated as a loss term. This can substantially increase the computational cost (particularly due to gradient evaluation) when dealing with deep and complex models. Furthermore, the number of control points, namely the locations at which the learning-bias loss terms are evaluated, has a significant impact on both computational cost and the effectiveness of prior injection. On the one hand, increasing the number of control points strengthens adherence to the governing equation; on the other hand, it raises computational demands. This trade-off must therefore be carefully considered and evaluated on a case-by-case basis. Ultimately, even if the weight of the learning bias loss terms could be tuned, a strict compliance of the model’s output with the governing equation cannot be guaranteed. For this reason, adopting both inductive and learning bias strategies jointly may be beneficial to inject prior domain knowledge more rigorously and robustly.

The proposed models define a general pipeline applicable to a wide range of environmental applications, where in situ measurements and spatially distributed data are jointly leveraged to predict a target variable, and where a governing equation, even if with some unknown parameters, is desirable to be incorporated. Physics-guided machine learning thus enables the development of hybrid hydrological and, more generally, Earth system models that combine the strengths of theory-driven and data-driven approaches, improving computational efficiency while retaining the flexibility to adapt to observed data. In this way, such models provide more effective tools for representing and predicting complex Earth system dynamics.

9 Future Works

Even though we obtained remarkable results, several research directions can be undertaken. First, given the widespread presence of missing and irregular data across many disciplines, a more extensive evaluation of alternative strategies for handling missing data would be valuable. For instance, attention-based mechanisms could be exploited to design masking strategies that avoid explicit imputation. In addition, alternative neural architectures could be explored to capture better complex and context-dependent relationships, such as Mixture-of-Experts [47].

In developing the proposed physics-guided strategies, a simple yet effective Euler integration scheme was adopted; however, future work could investigate Neural Differential Equation frameworks to assess more advanced numerical integration methods [48, 25]. While such approaches would increase computational demands, they could enable models to better learn the underlying dynamics and provide a more rigorous mathematical foundation for incorporating additional physical constraints (e.g., mass conservation).

Finally, future studies could benefit from the inclusion of additional data sources, including newly acquired groundwater level observations from the 2024 and 2025 field campaigns, as well as other spatially distributed datasets such as land-cover maps [49] or soil moisture products [50]. These data could offer more informative exogenous forcings, particularly for those related to anthropogenic activities (e.g., irrigation).

Author Contributions

Matteo Salis: Writing - original draft, review & editing, Investigation, Conceptualization, Visualization, Validation, Software, Methodology, Data curation, Resources. **Gabriele Sartor:** Supervision, Software, Investigation, Conceptualization, Resources. **Rosa Meo:** Supervision, Writing - review. **Stefano Ferraris:** Supervision, Conceptualization, , Writing - review. **Abdourrahmane M. Atto:** Supervision, Investigation, Conceptualization, Writing - review.

Acknowledgments

We acknowledge ISCRRA for awarding our *Deep Learning for Spatio Temporal Phenomena, application to environmental data* (DL4STP) project access to the LEONARDO supercomputer, owned by the EuroHPC Joint Undertaking, hosted by CINECA (Italy).

The authors declares that they have no conflict of interest to disclose.

The authors disclose the use of LLM-based tools for grammar and spelling.

Data & Code availability

All adopted data are freely accessible, in details the groundwater data at the ARPA website <https://shorturl.at/F3KzQ>, and ERA5-land at [10.24381/cds.e2161bac](https://cds.clm.cloudapps.ecmwf.int/datasets/data/era5-land/). The code is released in a GitHub repository at <https://github.com/Matteo-Salis/physics-guided-gwl> with additional animations (GIF) of the predictions over the test set.

Additional Materials

A Sensors Statistics and Time Series

In Table 4 we reported summary statistics for every sensor considered in the study. Figure 20 shows the time series plots of the other twenty-four sensors in addition to the four shown in Figure 2.

B Test Set Predictions

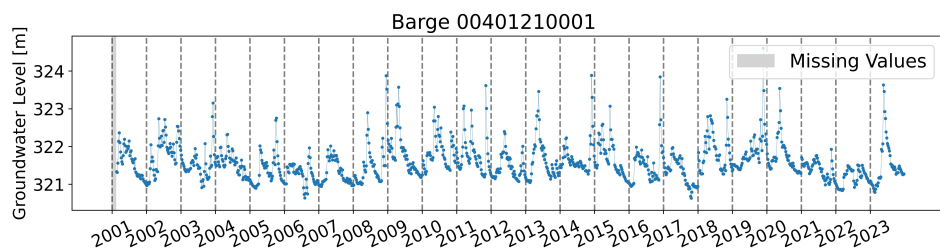
In Table 5, 6, 7, and 8 we reported the evaluation metrics computed on every sensor and every model in the iterative prediction (rollout) scenario. Furthermore, Figures 21 shows models rollout predictions in the test set for the other twenty-four sensors in addition to the four shown in Figure 7.

C Time Series Reconstruction

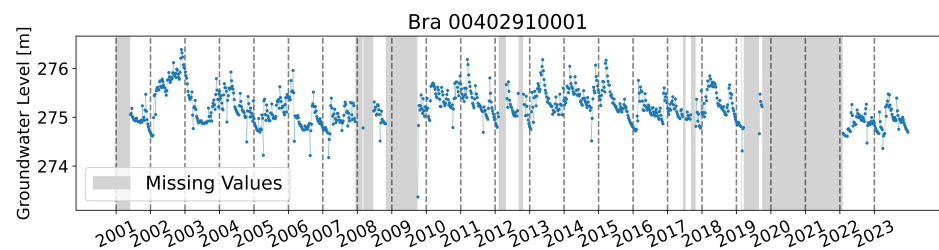
In Table 9, we reported the evaluation metrics for the reconstruction task of the PSTAINet-ILB model described in Section 7.4. Figure 22 depicts the weekly prediction from 01-01-2001 for the other twenty-four sensors in addition to the four shown in Figure 19.

Table 4: Summary statistics and percentage of missing data for each sensor.

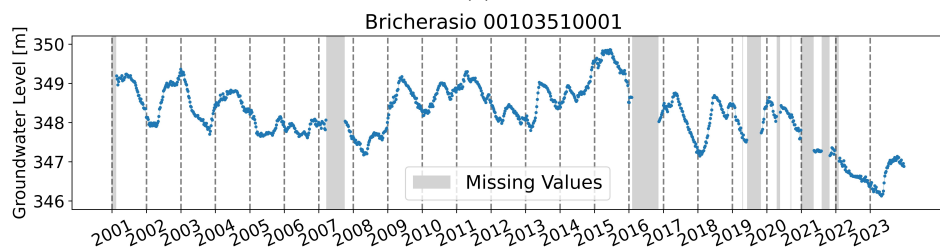
Sensor (Municipality - ID)	Mean [m]	Std. Dev. [m]	Missing (%)
Bricherasio - 00103510001	348.223	0.746	11.667
Buriasco - 00104110001	274.183	1.795	37.750
Candiolo - 00105110001	232.812	0.513	39.417
Carmagnola - 00105910001	231.893	0.813	3.500
Carmagnola - 00105910002	223.768	0.403	8.333
Cavour - 00107010001	274.777	1.842	22.000
Collegno - 00109010001	265.223	1.114	20.583
La Loggia - 00112710001	219.358	0.441	23.500
Orbassano - 00117110001	257.017	1.788	30.833
Poirino - 00119710001	237.157	0.544	76.917
Scalenghe - 00126010001	256.419	1.061	4.333
Torino - 00127210001	227.730	0.564	4.750
Torino - 00127210003	208.770	0.359	36.083
Virle - Piemonte 00131010001	241.877	0.585	32.500
Barge - 00401210001	321.579	0.488	0.583
Bra - 00402910001	275.202	0.341	22.583
Busca - 00403410001	434.676	1.862	24.917
Caramagna Piemonte - 00404110001	251.498	0.488	53.583
Cavallermaggiore - 00405910001	282.774	0.501	31.167
Cuneo - 00407810001	476.663	1.856	9.833
Fossano - 00408910001	351.209	0.485	14.417
Fossano - 00408910002	399.367	1.212	21.000
Moretta - 00414310002	249.211	0.348	13.083
Racconigi - 00417910001	252.498	0.744	5.833
Savigliano - 00421510001	312.866	0.266	21.833
Scarnafigi - 00421710001	282.321	1.169	31.833
Tarantasca - 00422510001	427.368	1.441	5.917
Vottignasco - 00425010001	380.387	0.834	26.750



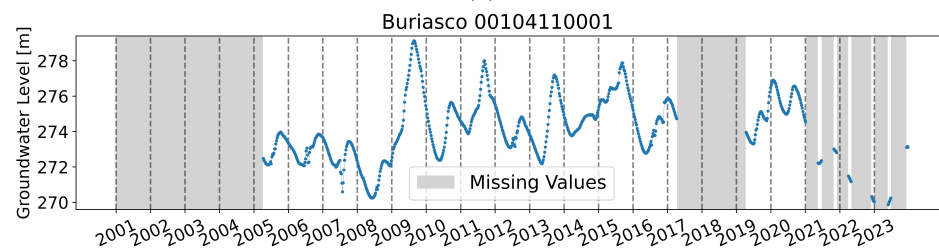
(a)



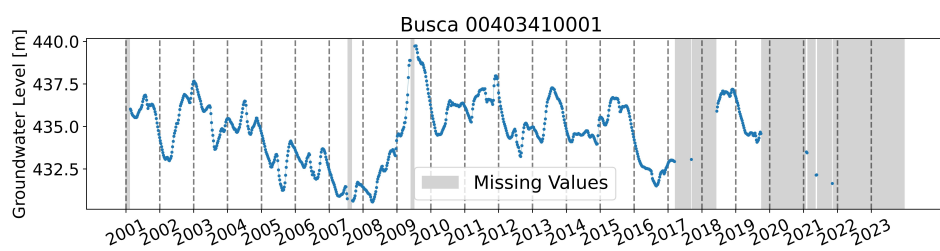
(b)



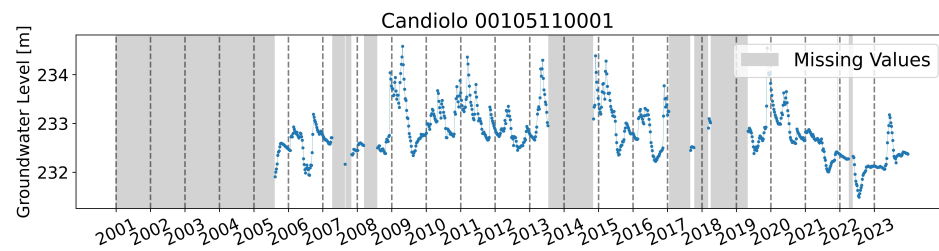
(c)



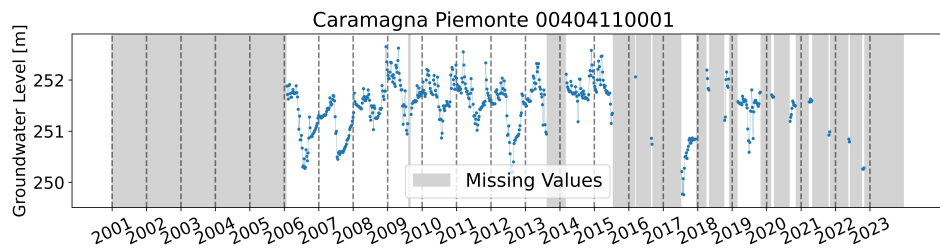
(d)



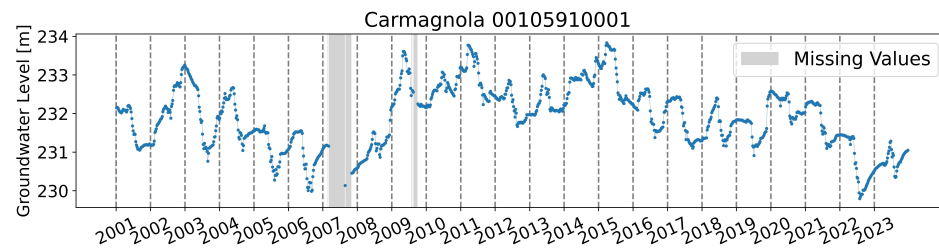
(e)



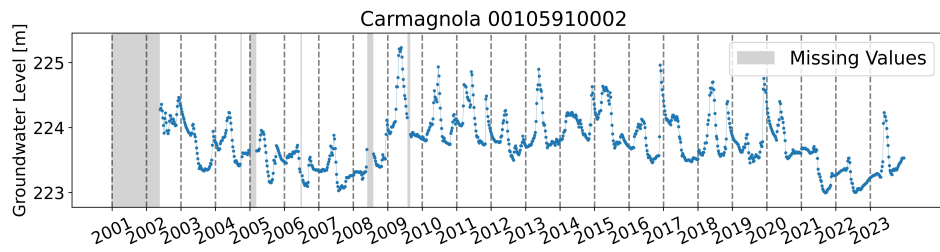
(f)



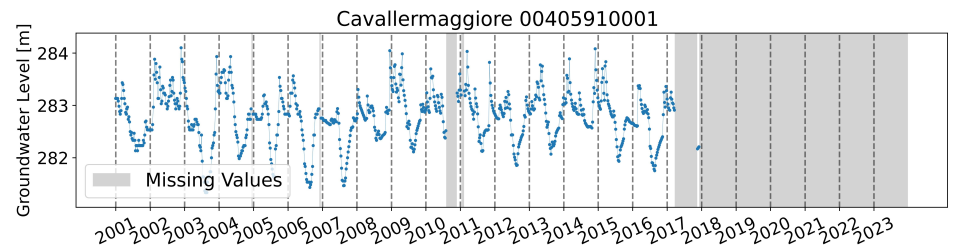
(g)



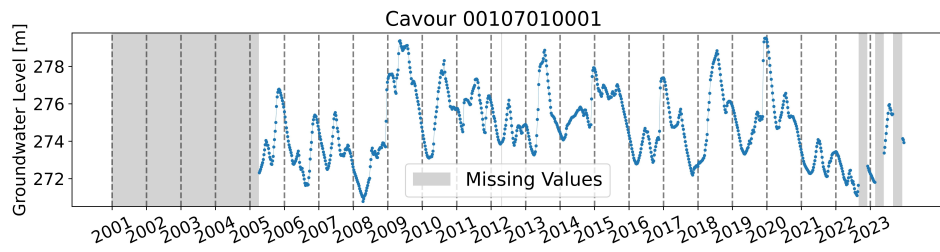
(h)



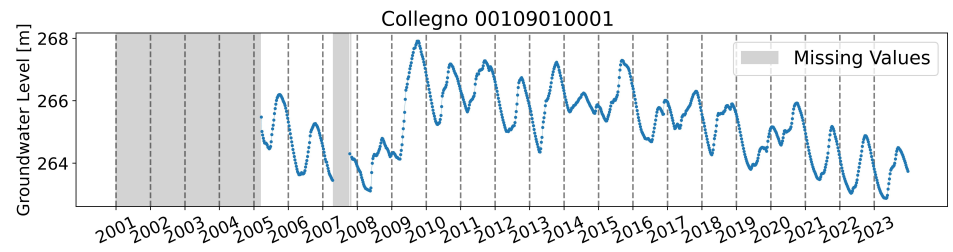
(i)



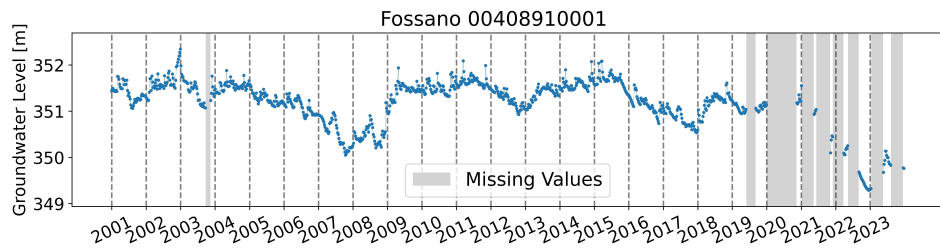
(j)



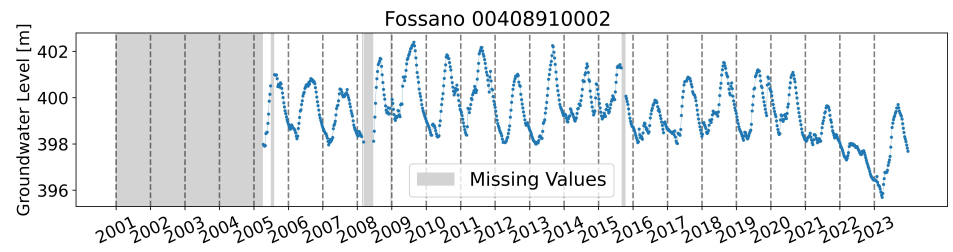
(k)



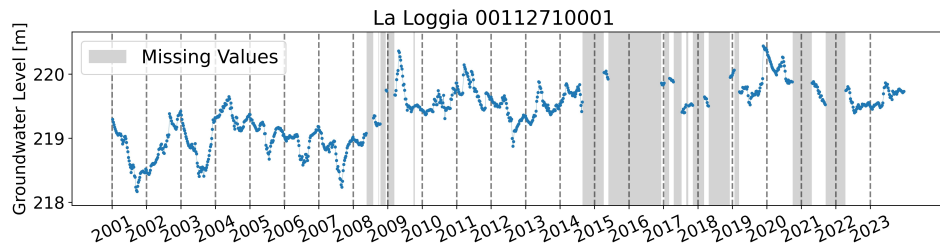
(l)



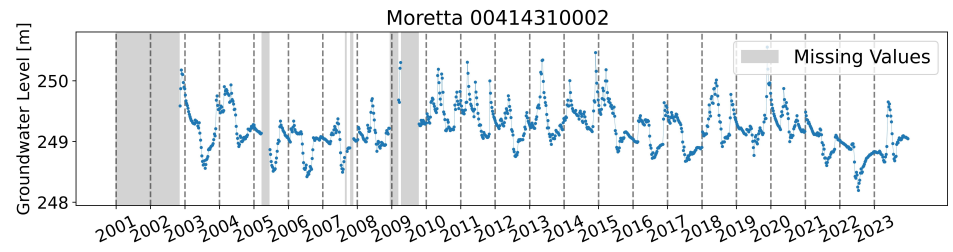
(m)



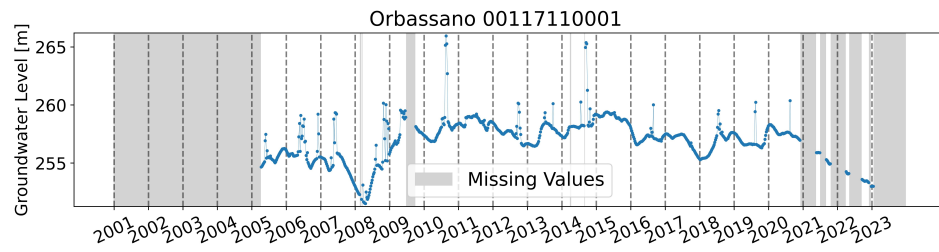
(n)



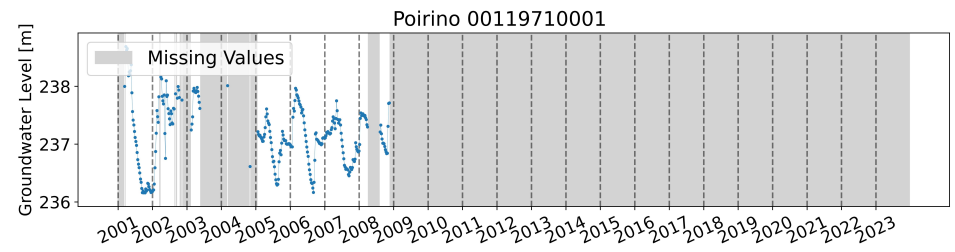
(o)



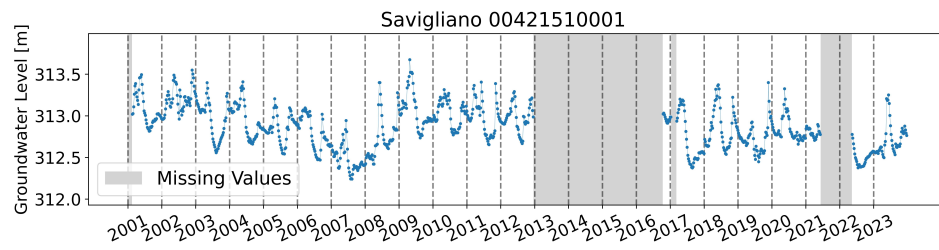
(p)



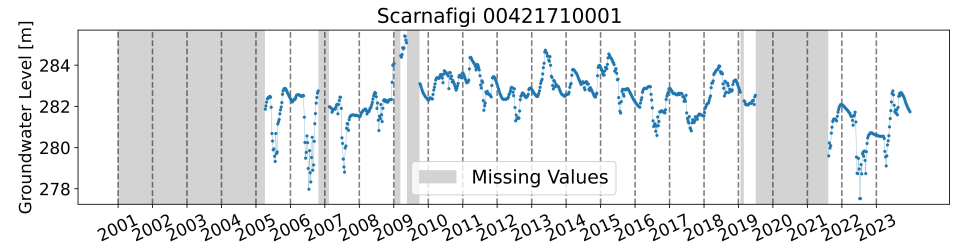
(q)



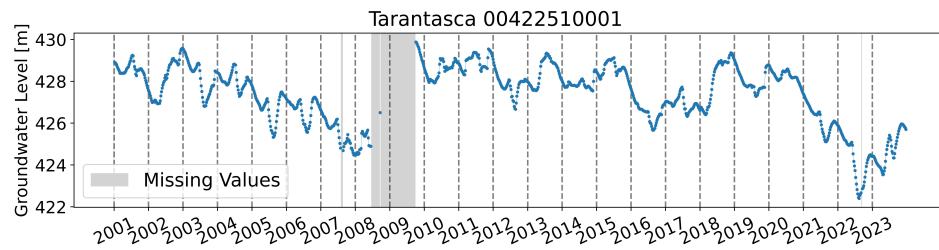
(r)



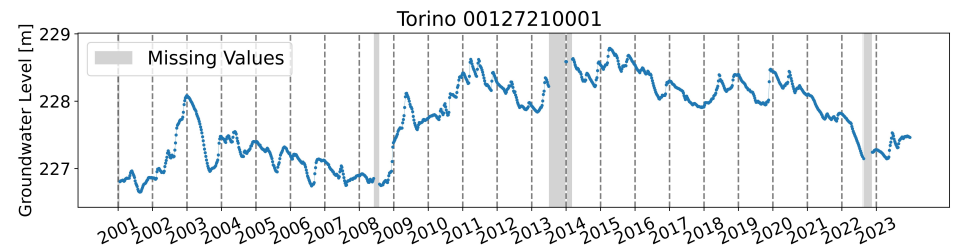
(s)



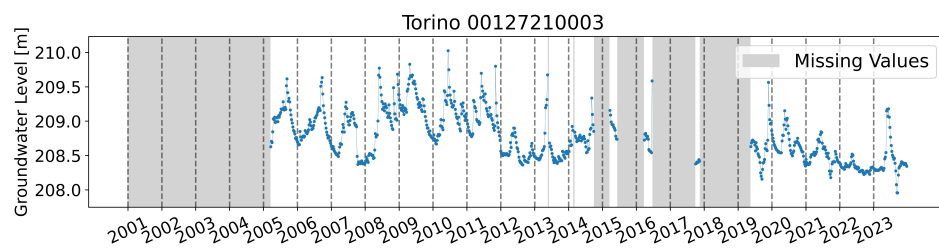
(t)



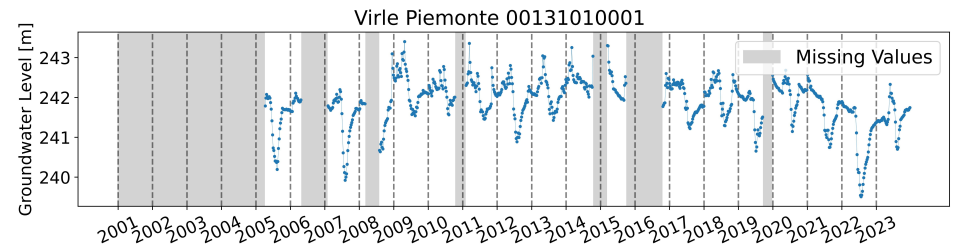
(u)



(v)



(w)



(x)

Figure 20: Groundwater level time series.

Table 5: STAINet metrics on the test set per sensor in the rollout setting.

Municipality Sensor	NBIAS	RMSE[m]	MAPE[%]	NSE	KGE
Bricherasio 00103510001	0.479	1.389	0.375	0.354	-0.016
Buriasco 00104110001	0.334	3.132	1.097	0.199	0.431
Candiolo 00105110001	0.149	0.564	0.205	0.440	0.328
Carmagnola 00105910001	0.236	1.029	0.400	0.406	0.293
Carmagnola 00105910002	0.085	0.330	0.122	0.625	0.366
Cavour 00107010001	0.171	2.175	0.657	0.210	0.258
Collegno 00109010001	0.283	1.472	0.515	0.268	0.224
La Loggia 00112710001	-0.214	0.624	0.234	-3.188	-1.148
Orbassano 00117110001	0.230	3.471	1.311	0.067	-0.801
Poirino 00119710001	-	-	-	-	-
Scalenghe 00126010001	0.315	1.708	0.625	0.288	0.577
Torino 00127210001	0.059	0.501	0.182	-0.640	-0.753
Torino 00127210003	0.089	0.450	0.162	0.181	-0.257
Virle Piemonte 00131010001	0.084	0.622	0.189	0.562	0.435
Barge 00401210001	-0.015	0.427	0.104	0.401	0.592
Bra 00402910001	-0.011	0.360	0.098	0.136	-0.116
Busca 00403410001	-	-	-	-	-
Caramagna Piemonte 00404110001	0.248	0.835	0.287	0.374	-0.534
Cavallermaggiore 00405910001	-	-	-	-	-
Cuneo 00407810001	0.314	2.525	0.498	0.330	0.740
Fossano 00408910001	0.608	1.491	0.399	0.106	-0.188
Fossano 00408910002	0.392	2.034	0.450	0.144	0.499
Moretta 00414310002	0.030	0.279	0.092	0.644	0.442
Racconigi 00417910001	0.102	0.789	0.252	0.424	0.210
Savigliano 00421510001	0.023	0.225	0.057	0.523	0.312
Scarnafigi 00421710001	0.141	1.561	0.458	0.323	0.218
Tarantasca 00422510001	0.499	2.974	0.637	0.162	0.031
Vottignasco 00425010001	0.234	1.353	0.285	0.058	-0.094

Table 6: PSTAINet-IB metrics on the test set per sensor in the rollout setting.

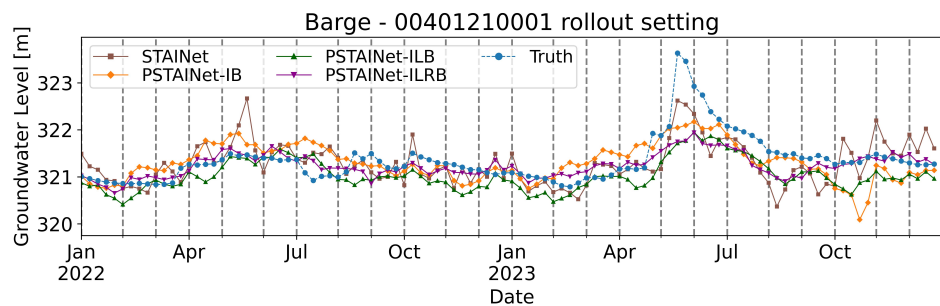
Municipality Sensor	NBIAS	RMSE[m]	MAPE[%]	NSE	KGE
Bricherasio 00103510001	0.517	1.482	0.406	0.265	-0.165
Buriasco 00104110001	0.200	2.078	0.675	0.647	0.074
Candiolo 00105110001	0.098	0.380	0.128	0.745	0.618
Carmagnola 00105910001	0.183	0.829	0.318	0.614	0.497
Carmagnola 00105910002	0.017	0.183	0.066	0.885	0.742
Cavour 00107010001	0.047	1.269	0.391	0.731	0.183
Collegno 00109010001	0.172	0.934	0.314	0.705	0.667
La Loggia 00112710001	-0.188	0.506	0.201	-1.755	-0.575
Orbassano 00117110001	0.086	1.372	0.491	0.854	-0.392
Poirino 00119710001	-	-	-	-	-
Scalenghe 00126010001	0.256	1.448	0.507	0.489	0.564
Torino 00127210001	0.014	0.397	0.142	-0.031	-0.296
Torino 00127210003	0.285	0.613	0.261	-0.519	0.167
Virle Piemonte 00131010001	0.077	0.441	0.151	0.779	0.746
Barge 00401210001	-0.011	0.422	0.100	0.414	0.520
Bra 00402910001	0.043	0.252	0.072	0.576	0.437
Busca 00403410001	-	-	-	-	-
Caramagna Piemonte 00404110001	0.250	0.734	0.289	0.517	0.798
Cavallermaggiore 00405910001	-	-	-	-	-
Cuneo 00407810001	0.202	1.809	0.340	0.656	0.767
Fossano 00408910001	0.389	0.943	0.256	0.642	0.582
Fossano 00408910002	0.324	1.658	0.366	0.432	0.568
Moretta 00414310002	0.056	0.270	0.089	0.666	0.604
Racconigi 00417910001	0.080	0.654	0.226	0.604	0.361
Savigliano 00421510001	-0.071	0.199	0.049	0.627	0.643
Scarnafigi 00421710001	0.069	1.284	0.391	0.542	0.149
Tarantasca 00422510001	0.261	1.715	0.344	0.721	0.063
Vottignasco 00425010001	0.047	0.645	0.142	0.786	0.596

Table 7: PSTAINet-ILB metrics on the test set per sensor in the rollout setting.

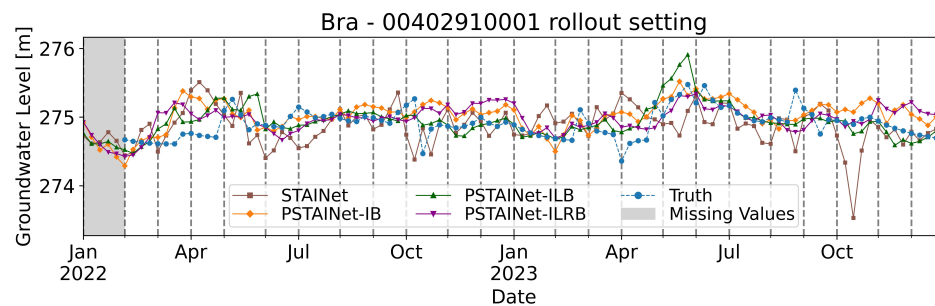
Municipality Sensor	NBIAS	RMSE[m]	MAPE[%]	NSE	KGE
Bricherasio 00103510001	0.276	0.795	0.216	0.788	0.531
Buriasco 00104110001	0.089	1.230	0.363	0.877	0.403
Candiolo 00105110001	-0.122	0.418	0.143	0.692	0.567
Carmagnola 00105910001	0.021	0.444	0.154	0.889	0.331
Carmagnola 00105910002	-0.065	0.253	0.095	0.779	0.675
Cavour 00107010001	-0.037	1.234	0.328	0.746	0.298
Collegno 00109010001	-0.001	0.312	0.094	0.967	0.855
La Loggia 00112710001	-0.399	0.928	0.413	-8.280	-0.045
Orbassano 00117110001	0.013	0.576	0.203	0.974	-0.204
Poirino 00119710001	-	-	-	-	-
Scalenghe 00126010001	0.070	0.600	0.182	0.912	0.745
Torino 00127210001	-0.378	0.866	0.355	-3.899	0.069
Torino 00127210003	-0.065	0.366	0.141	0.459	-0.005
Virle Piemonte 00131010001	-0.043	0.433	0.144	0.788	0.690
Barge 00401210001	-0.079	0.454	0.109	0.324	0.585
Bra 00402910001	0.014	0.201	0.054	0.731	0.580
Busca 00403410001	-	-	-	-	-
Caramagna Piemonte 00404110001	0.236	0.690	0.273	0.573	0.870
Cavallermaggiore 00405910001	-	-	-	-	-
Cuneo 00407810001	0.075	0.933	0.169	0.908	0.835
Fossano 00408910001	0.248	0.603	0.163	0.854	0.611
Fossano 00408910002	0.286	1.549	0.327	0.504	0.561
Moretta 00414310002	-0.005	0.199	0.065	0.819	0.630
Racconigi 00417910001	-0.001	0.447	0.160	0.815	0.468
Savigliano 00421510001	-0.118	0.226	0.058	0.519	0.689
Scarnafigi 00421710001	0.012	1.155	0.337	0.629	0.188
Tarantasca 00422510001	0.034	0.753	0.155	0.946	0.603
Vottignasco 00425010001	0.036	0.585	0.122	0.824	0.635

Table 8: PSTAINet-ILRB metrics on the test set per sensor in the rollout setting.

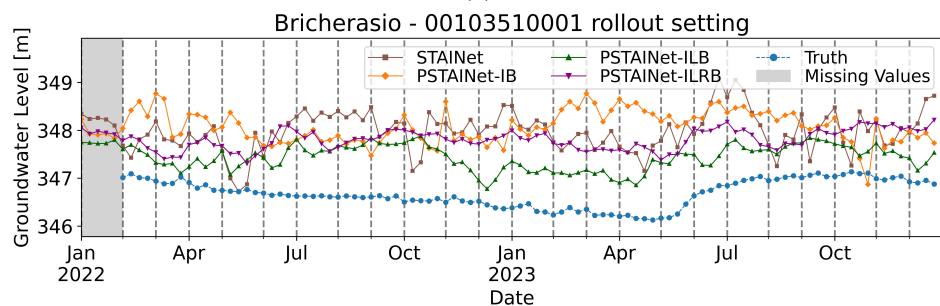
Municipality Sensor	NBIAS	RMSE[m]	MAPE[%]	NSE	KGE
Bricherasio 00103510001	0.415	1.161	0.325	0.548	0.295
Buriasco 00104110001	0.160	1.889	0.544	0.709	0.441
Candiolo 00105110001	0.069	0.357	0.134	0.775	0.496
Carmagnola 00105910001	0.053	0.524	0.195	0.846	0.424
Carmagnola 00105910002	-0.083	0.297	0.108	0.695	0.552
Cavour 00107010001	-0.014	1.317	0.368	0.710	0.228
Collegno 00109010001	0.061	0.678	0.193	0.844	0.407
La Loggia 00112710001	-0.345	0.840	0.357	-6.607	-0.585
Orbassano 00117110001	0.099	1.777	0.618	0.756	-0.995
Poirino 00119710001	-	-	-	-	-
Scalenghe 00126010001	0.231	1.311	0.458	0.581	0.671
Torino 00127210001	-0.188	0.608	0.230	-1.411	-0.599
Torino 00127210003	0.157	0.511	0.174	-0.057	-0.285
Virle Piemonte 00131010001	0.050	0.481	0.165	0.738	0.702
Barge 00401210001	-0.028	0.378	0.074	0.530	0.422
Bra 00402910001	0.025	0.243	0.069	0.606	0.258
Busca 00403410001	-	-	-	-	-
Caramagna Piemonte 00404110001	0.114	0.522	0.176	0.756	-0.601
Cavallermaggiore 00405910001	-	-	-	-	-
Cuneo 00407810001	0.221	1.809	0.355	0.656	0.815
Fossano 00408910001	0.433	1.085	0.285	0.527	-0.528
Fossano 00408910002	0.295	1.560	0.337	0.497	0.626
Moretta 00414310002	-0.031	0.250	0.083	0.714	0.609
Racconigi 00417910001	0.039	0.546	0.183	0.724	0.321
Savigliano 00421510001	-0.003	0.169	0.045	0.732	0.675
Scarnafigi 00421710001	0.068	1.225	0.362	0.583	0.182
Tarantasca 00422510001	0.256	1.641	0.328	0.745	0.316
Vottignasco 00425010001	0.116	0.760	0.156	0.702	0.618



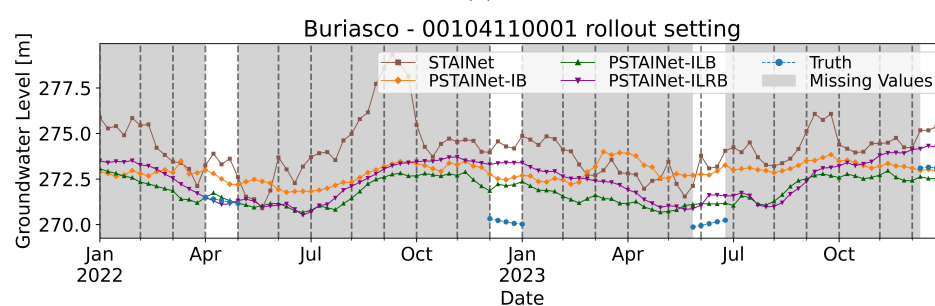
(a)



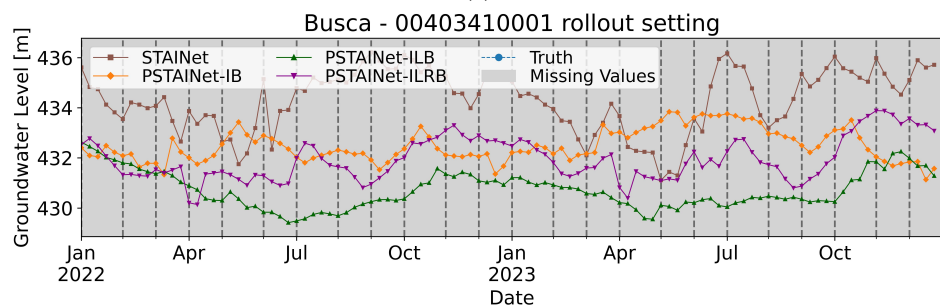
(b)



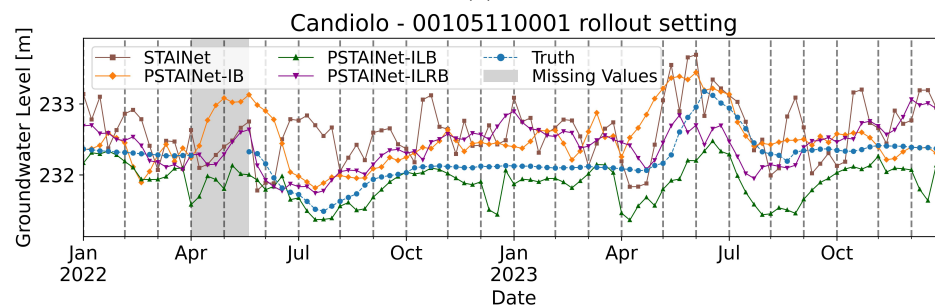
(c)



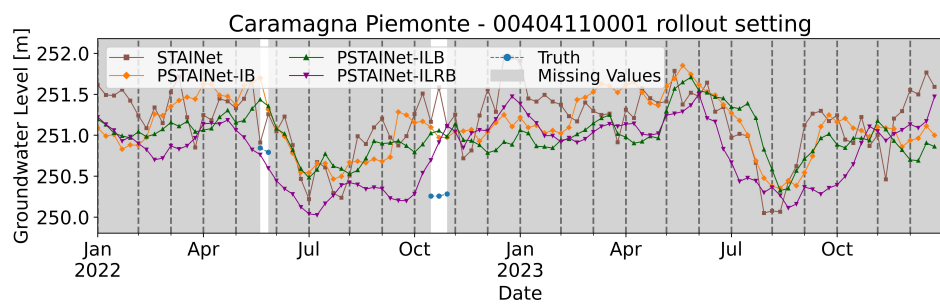
(d)



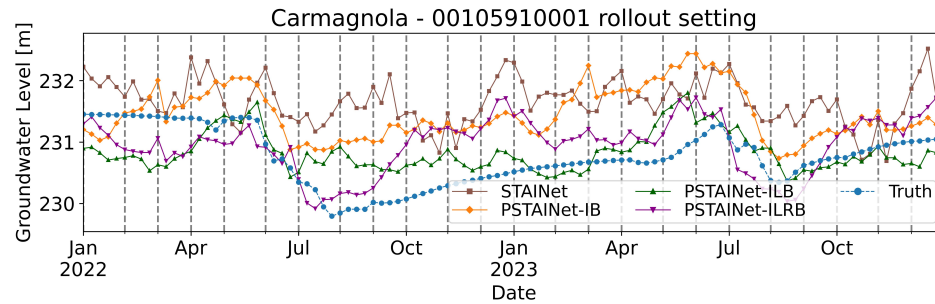
(e)



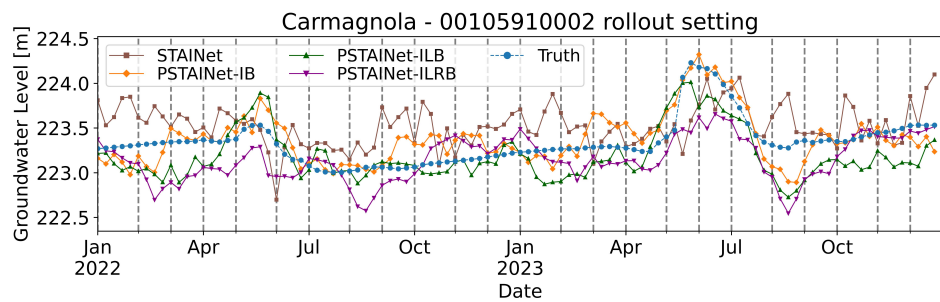
(f)



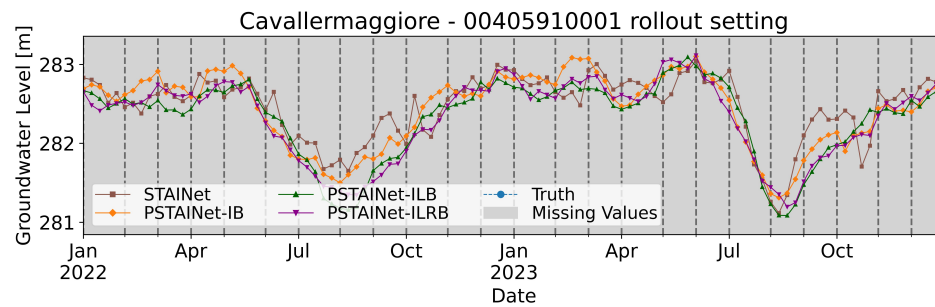
(g)



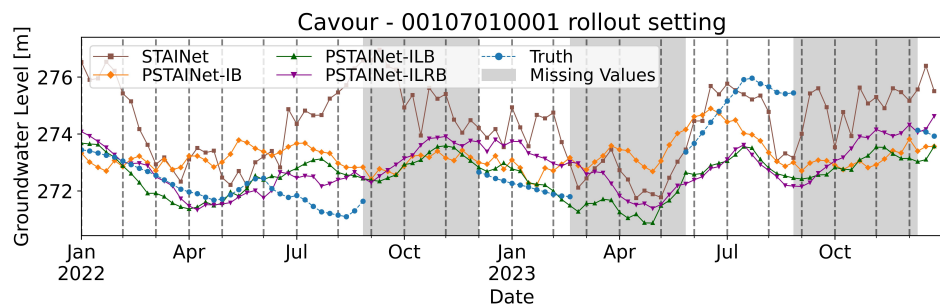
(h)



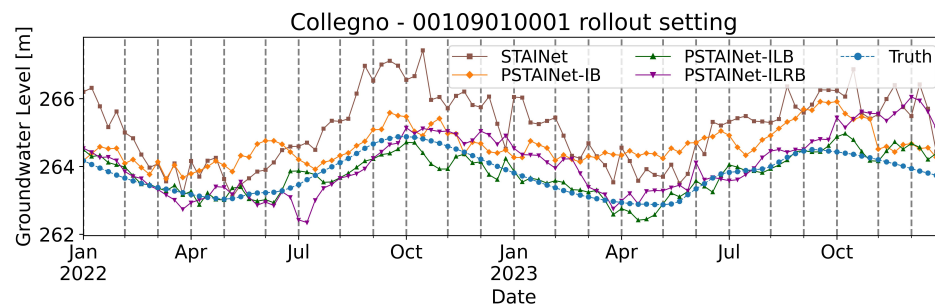
(i)



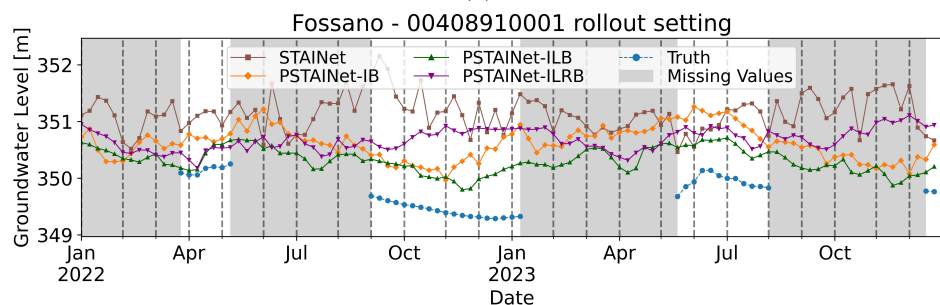
(j)



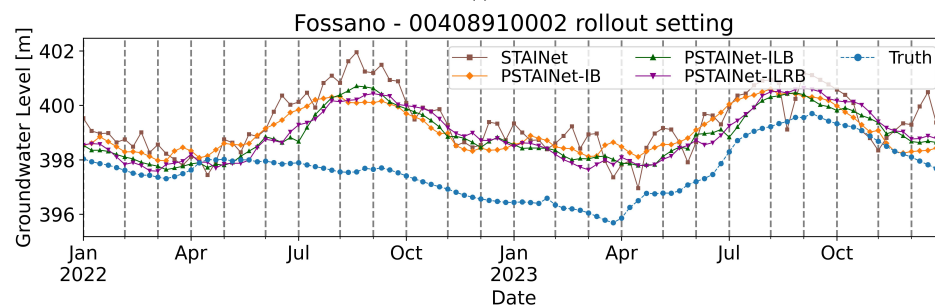
(k)



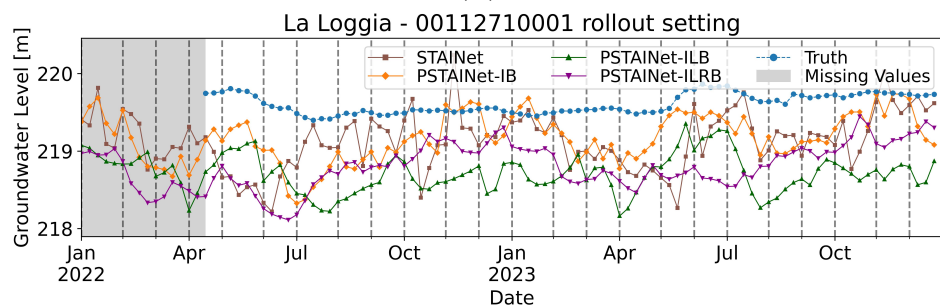
(l)



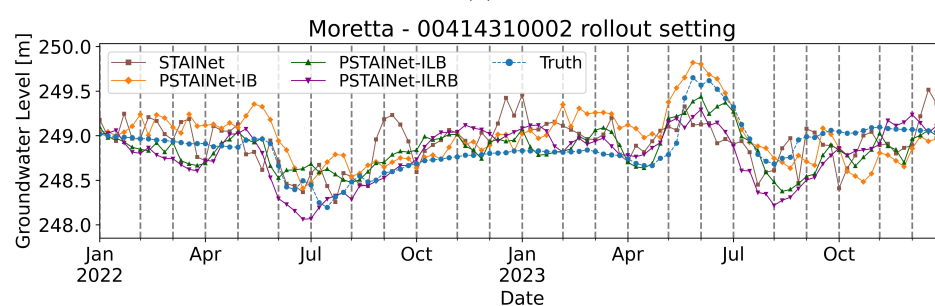
(m)



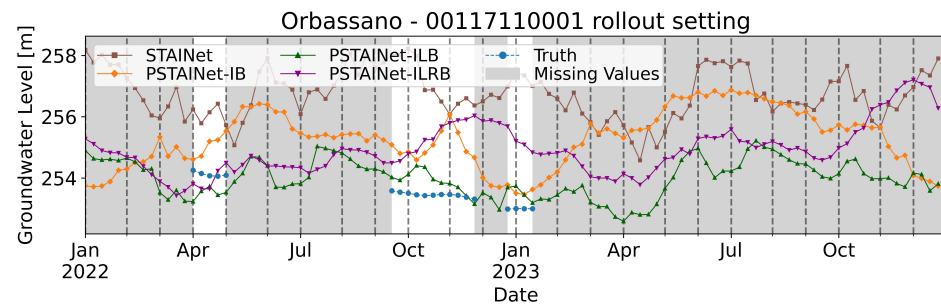
(n)



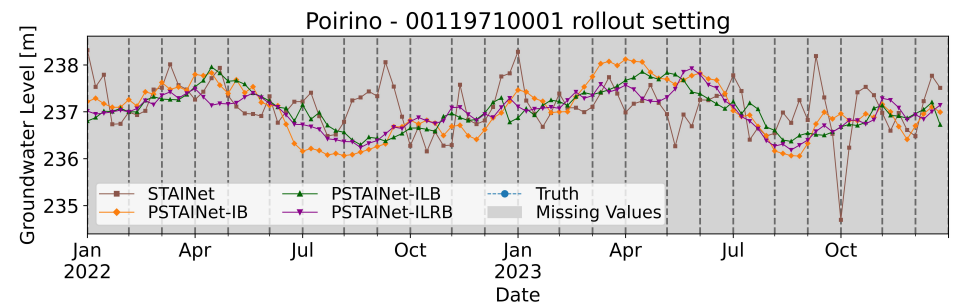
(o)



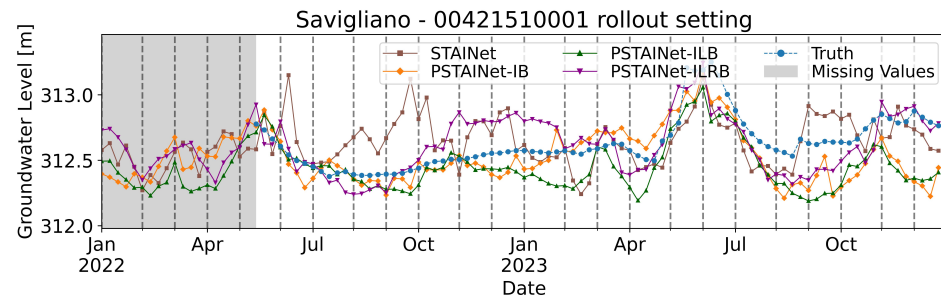
(p)



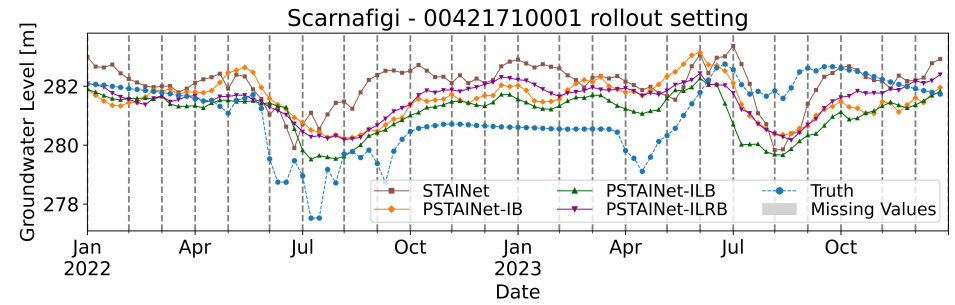
(q)



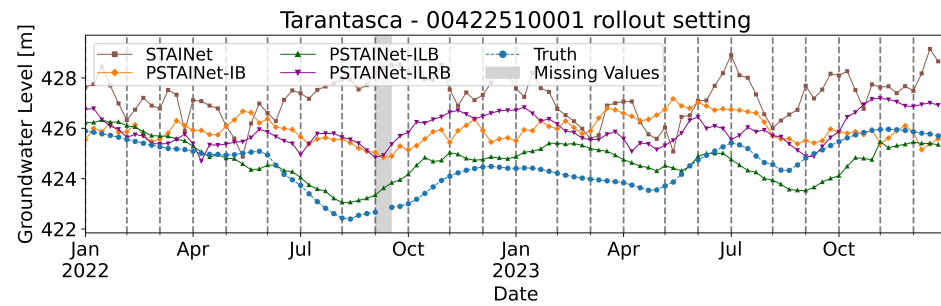
(r)



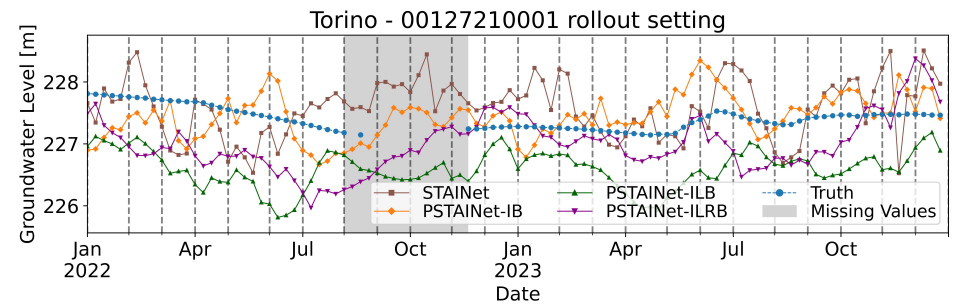
(s)



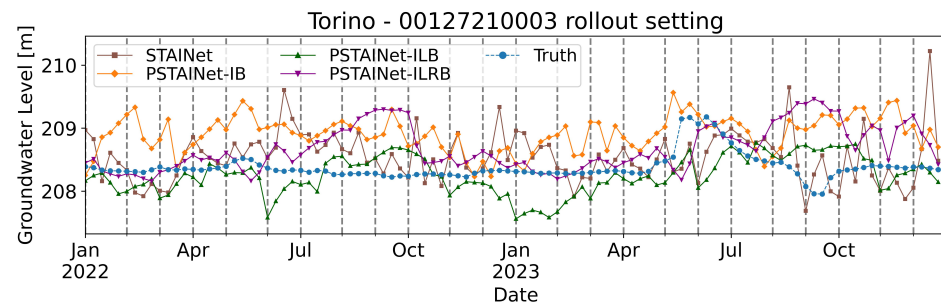
(t)



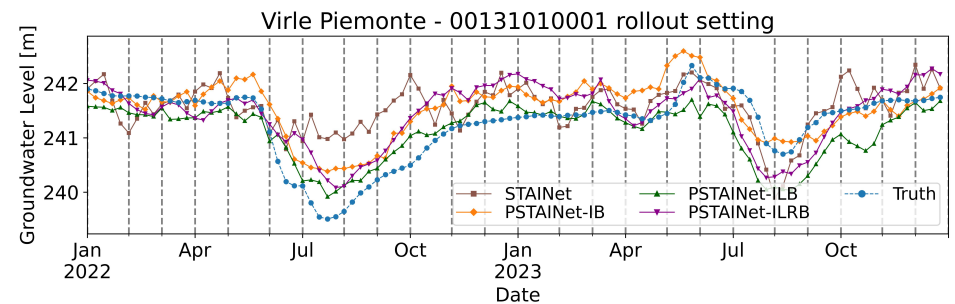
(u)



(v)



(w)

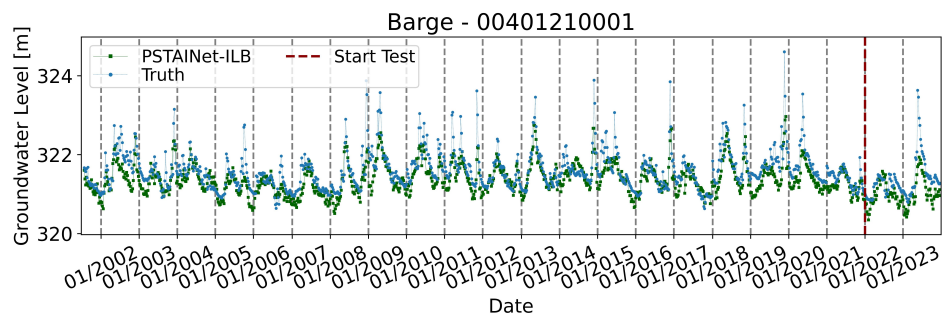


(x)

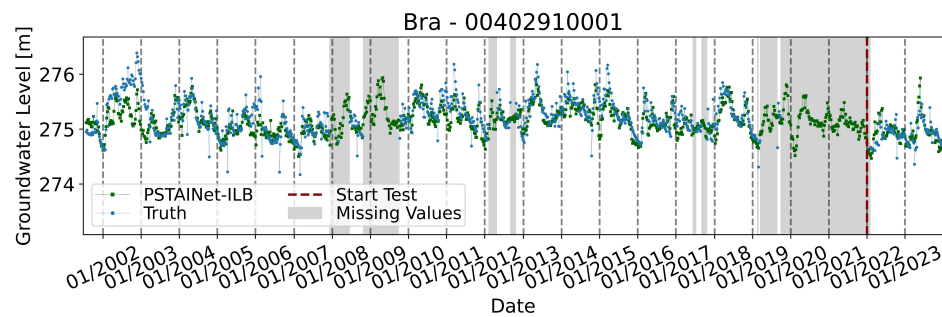
Figure 21: Test set predictions in the rollout setting.

Table 9: PSTAINet-ILB reconstruction metrics per sensor in the rollout setting.

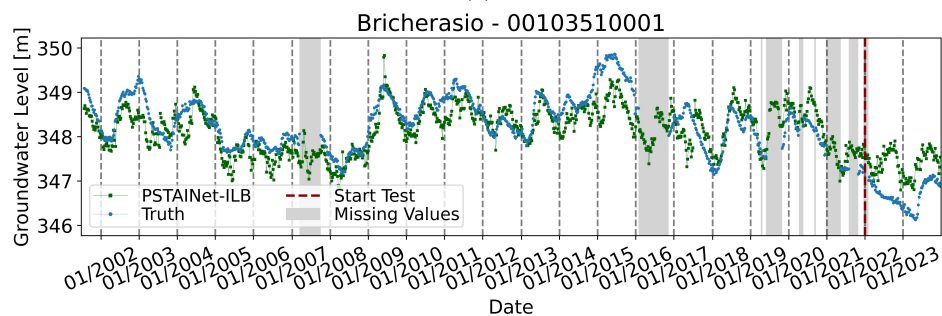
Municipality Sensor	NBIAS	RMSE[m]	MAPE[%]	NSE	KGE
Bricherasio 00103510001	-0.030	0.451	0.103	0.651	0.659
Buriasco 00104110001	-0.035	0.920	0.264	0.737	0.852
Candiolo 00105110001	-0.123	0.433	0.148	0.311	0.760
Carmagnola 00105910001	-0.038	0.471	0.165	0.677	0.727
Carmagnola 00105910002	-0.090	0.294	0.106	0.475	0.785
Cavour 00107010001	-0.026	1.131	0.313	0.624	0.765
Collegno 00109010001	-0.015	0.577	0.163	0.738	0.872
La Loggia 00112710001	-0.118	0.488	0.176	-0.215	0.368
Orbassano 00117110001	-0.033	1.213	0.309	0.540	0.724
Poirino 00119710001	-0.030	0.339	0.107	0.548	0.743
Scalenghe 00126010001	-0.018	0.472	0.149	0.807	0.807
Torino 00127210001	-0.120	0.542	0.191	0.042	0.629
Torino 00127210003	-0.125	0.424	0.161	-0.360	0.375
Virle Piemonte 00131010001	-0.058	0.339	0.112	0.671	0.820
Barge 00401210001	-0.057	0.377	0.087	0.407	0.709
Bra 00402910001	-0.025	0.257	0.066	0.442	0.602
Busca 00403410001	-0.024	1.154	0.196	0.621	0.792
Caramagna Piemonte 00404110001	-0.021	0.311	0.096	0.593	0.661
Cavallermaggiore 00405910001	-0.025	0.262	0.069	0.732	0.769
Cuneo 00407810001	0.003	0.928	0.148	0.760	0.872
Fossano 00408910001	-0.080	0.355	0.085	0.484	0.671
Fossano 00408910002	0.004	0.740	0.135	0.638	0.750
Moretta 00414310002	-0.016	0.175	0.055	0.749	0.840
Racconigi 00417910001	-0.023	0.447	0.141	0.651	0.655
Savigliano 00421510001	-0.079	0.200	0.052	0.423	0.768
Scarnafigi 00421710001	-0.011	0.644	0.169	0.704	0.709
Tarantasca 00422510001	0.001	0.774	0.140	0.725	0.856
Vottignasco 00425010001	0.015	0.421	0.084	0.752	0.793



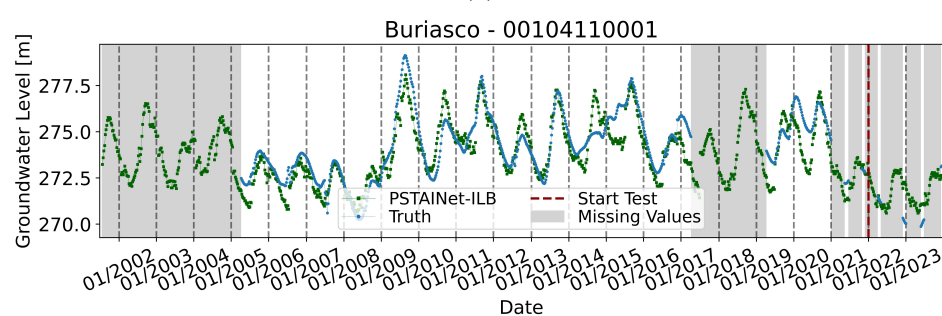
(a)



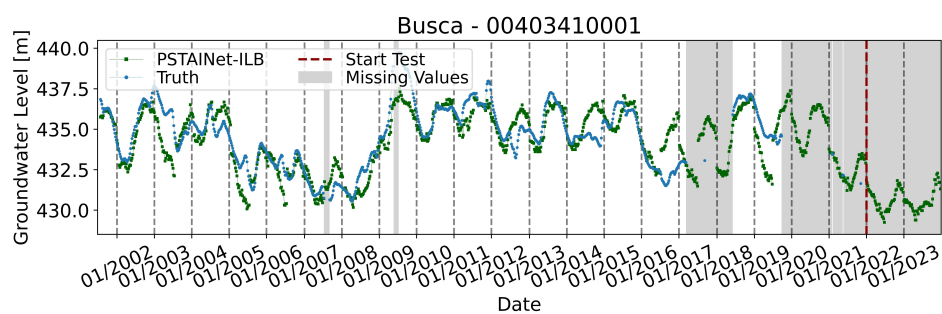
(b)



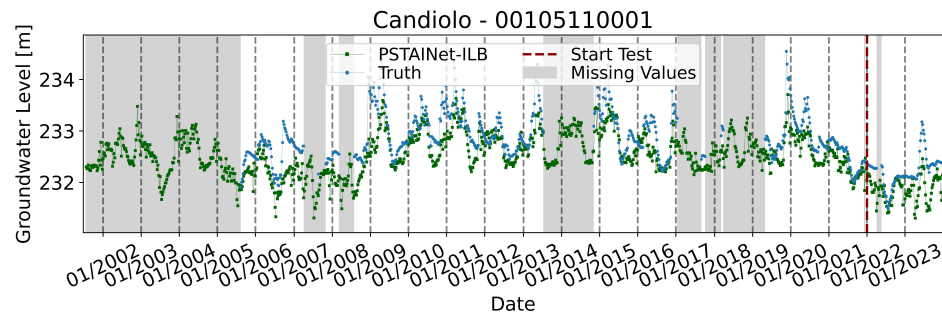
(c)



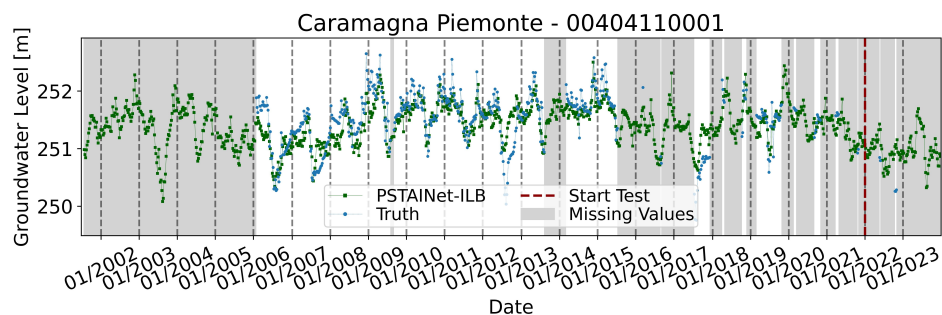
(d)



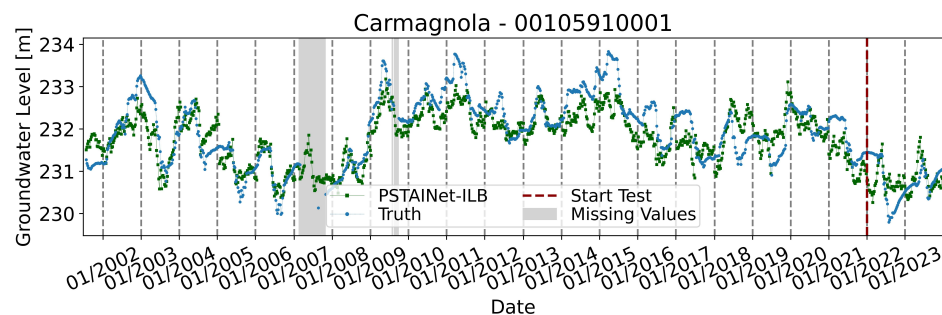
(e)



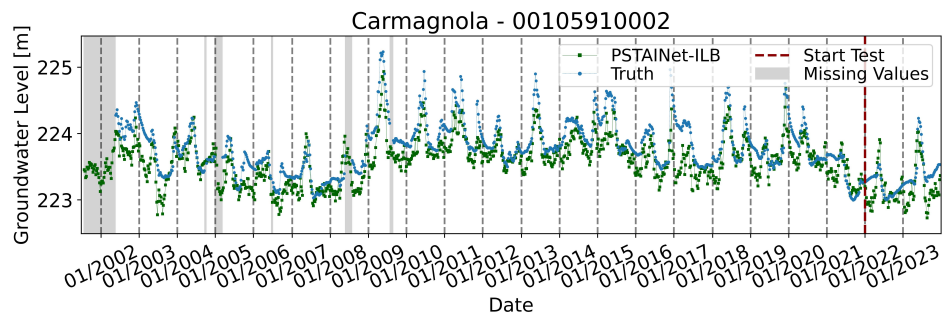
(f)



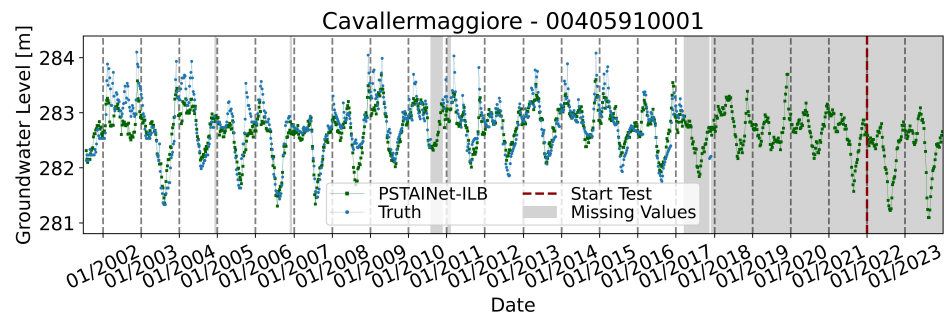
(g)



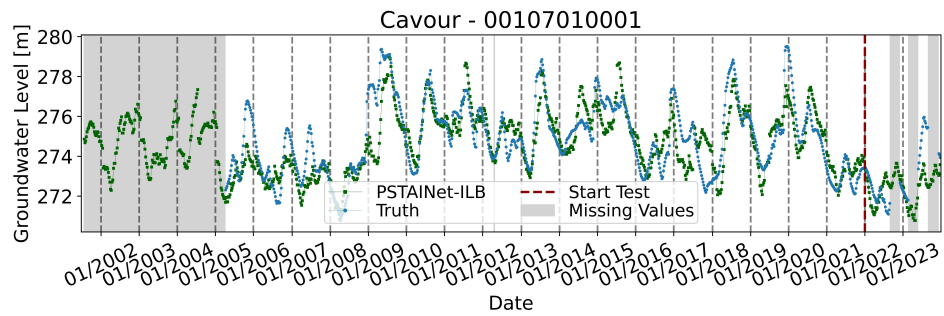
(h)



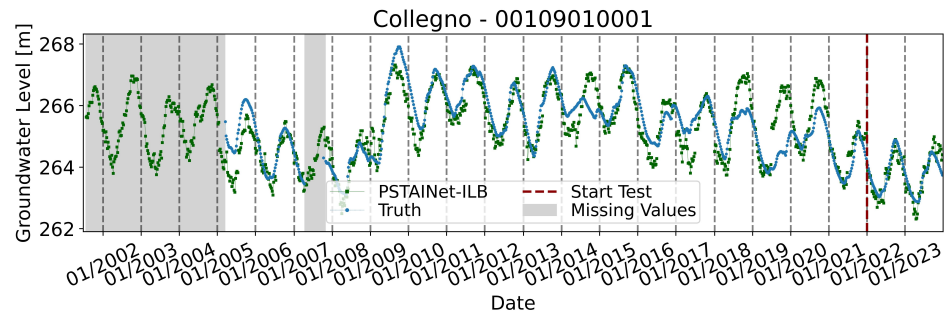
(i)



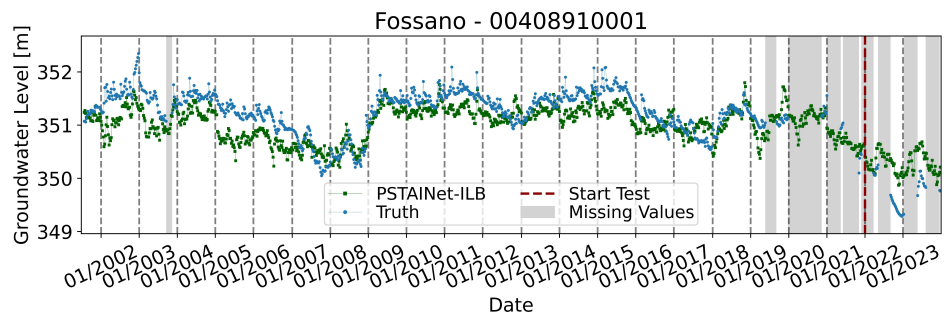
(j)



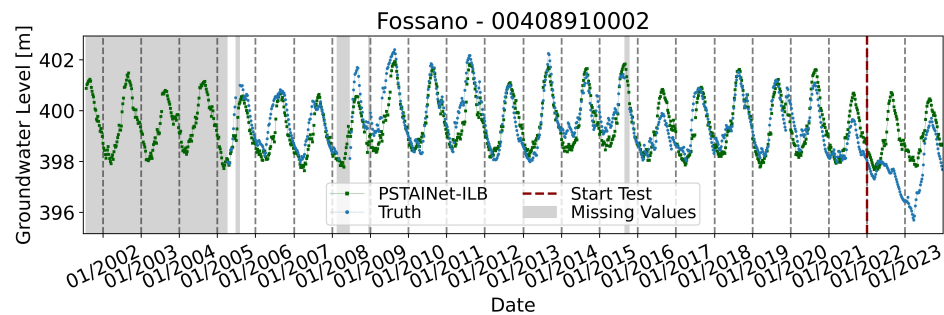
(k)



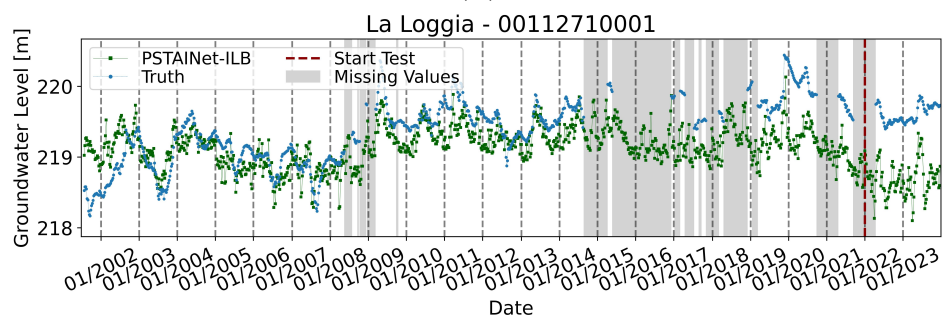
(l)



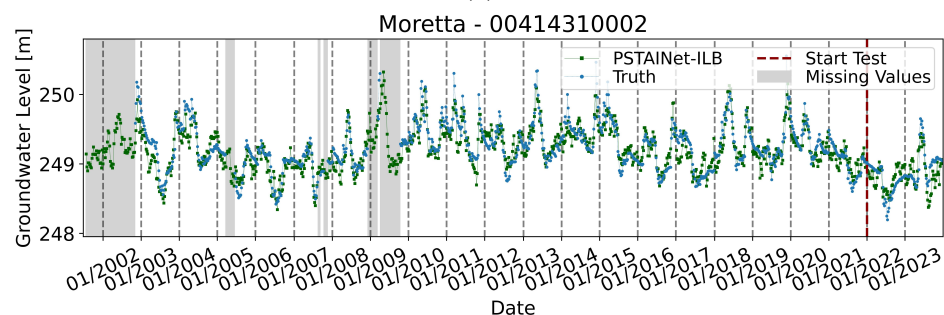
(m)



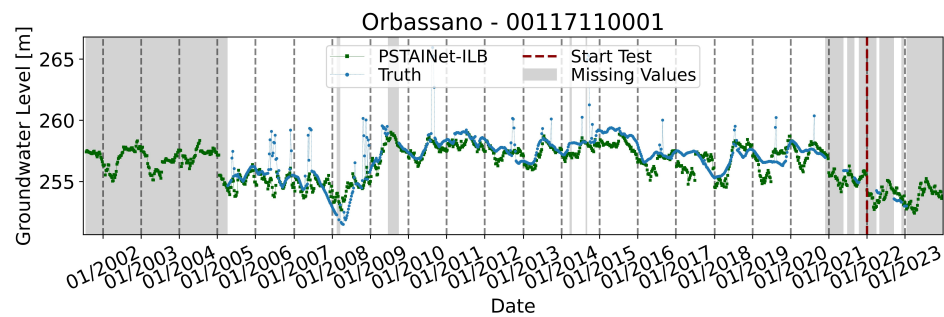
(n)



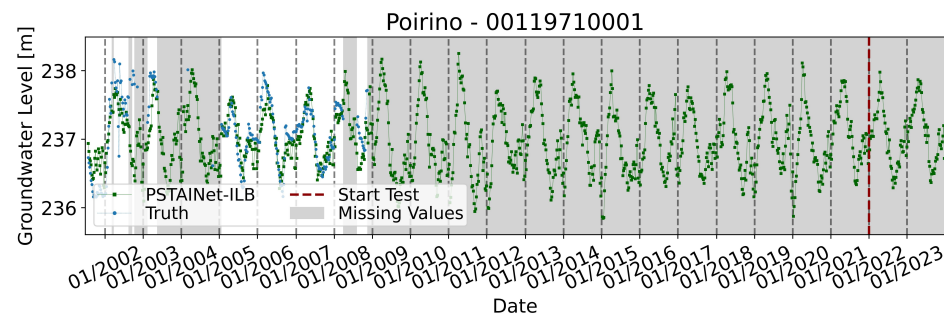
(o)



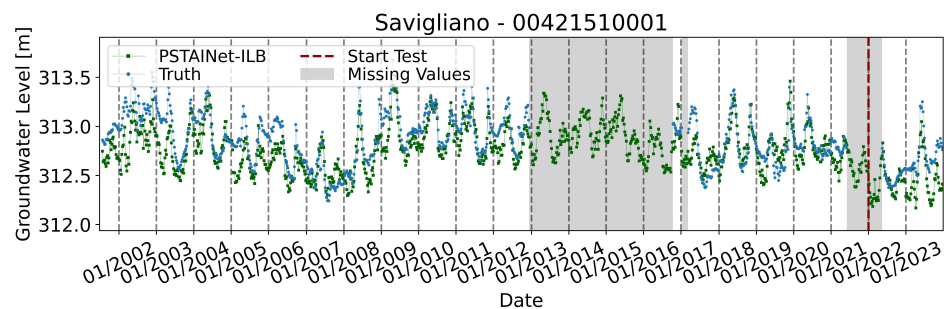
(p)



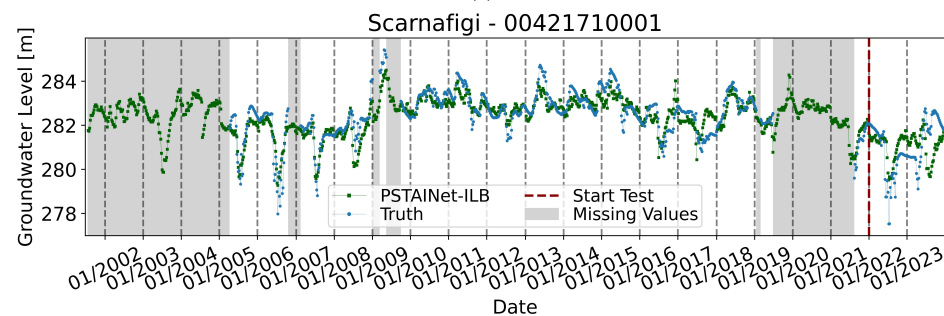
(q)



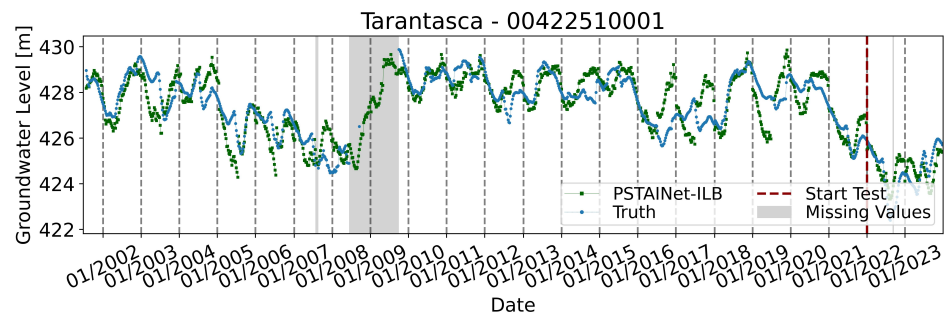
(r)



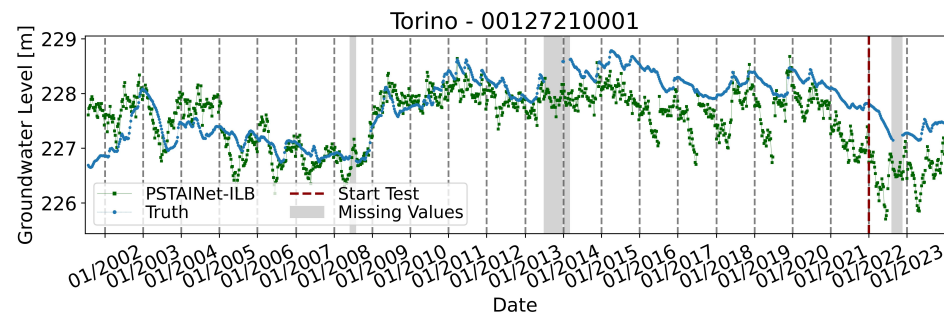
(s)



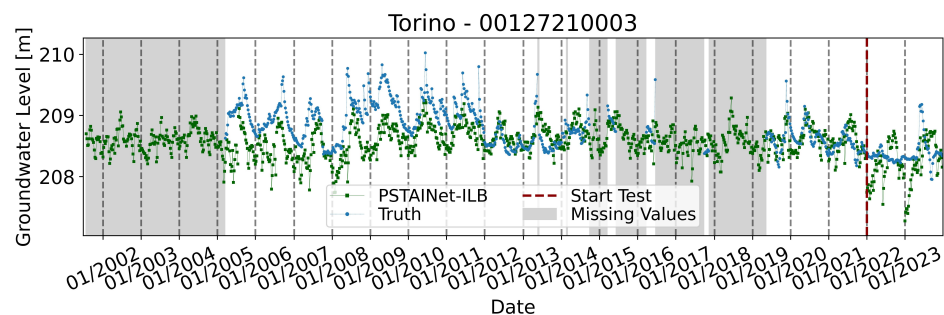
(t)



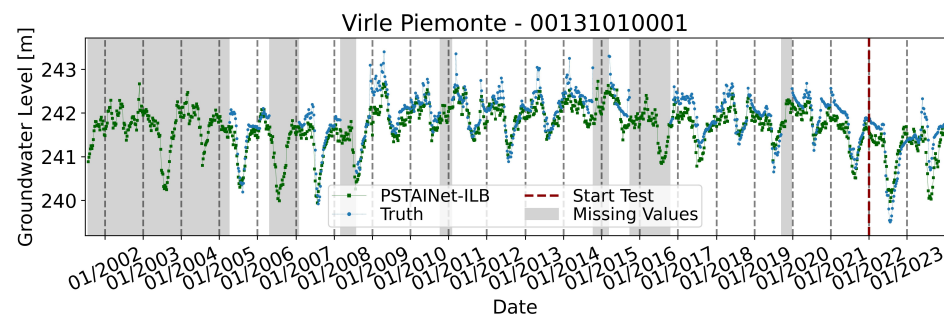
(u)



(v)



(w)



(x)

Figure 22: Test set predictions in the rollout setting.

References

- [1] H. Tao, M. M. Hameed, H. A. Marhoon, M. Zounemat-Kermani, S. Heddami, S. Kim, S. O. Sulaiman, M. L. Tan, Z. Sa'adi, A. D. Mehr, M. F. Allawi, S. Abba, J. M. Zain, M. W. Falah, M. Jamei, N. D. Bokde, M. Bayatvarkeshi, M. Al-Mukhtar, S. K. Bhagat, T. Tiyasha, K. M. Khedher, N. Al-Ansari, S. Shahid, Z. M. Yaseen, [Groundwater level prediction using machine learning models: A comprehensive review](#), *Neurocomputing* 489 (2022) 271–308. doi:10.1016/j.neucom.2022.03.014.
URL <https://linkinghub.elsevier.com/retrieve/pii/S092523122200282X>
- [2] M. G. Zanoni, B. Majone, A. Bellin, A catchment-scale model of river water quality by Machine Learning, *Science of The Total Environment* 838 (2022) 156377. doi:10.1016/j.scitotenv.2022.156377.
- [3] M. Andrychowicz, L. Espeholt, D. Li, S. Merchant, A. Merose, F. Zyda, S. Agrawal, N. Kalchbrenner, Deep Learning for Day Forecasts from Sparse Observations, <http://arxiv.org/abs/2306.06079> (2023).
- [4] R. Lam, A. Sanchez-Gonzalez, M. Willson, P. Wirnsberger, M. Fortunato, F. Alet, S. Ravuri, T. Ewalds, Z. Eaton-Rosen, W. Hu, A. Merose, S. Hoyer, G. Holland, O. Vinyals, J. Stott, A. Pritzel, S. Mohamed, P. Battaglia, [GraphCast: Learning skillful medium-range global weather forecasting](#) (2023). doi:10.48550/arXiv.2212.12794.
URL <http://arxiv.org/abs/2212.12794>
- [5] A. Karpatne, G. Atluri, J. H. Faghmous, M. Steinbach, A. Banerjee, A. Ganguly, S. Shekhar, N. Samatova, V. Kumar, Theory-Guided Data Science: A New Paradigm for Scientific Discovery from Data, *IEEE Transactions on Knowledge and Data Engineering* 29 (10) (2017) 2318–2331. doi:10.1109/TKDE.2017.2720168.
- [6] A. Daw, A. Karpatne, W. D. Watkins, J. S. Read, V. Kumar, [Physics-Guided Neural Networks \(PGNN\): An Application in Lake Temperature Modeling](#), Chapman and Hall/CRC, 2022, p. 353–372. doi:10.1201/9781003143376-15.
URL <http://dx.doi.org/10.1201/9781003143376-15>
- [7] J. Willard, X. Jia, S. Xu, M. Steinbach, V. Kumar, Integrating Scientific Knowledge with Machine Learning for Engineering and Environmental Systems, *ACM Comput. Surv.* 55 (4) (2022) 66:1–66:37. doi:10.1145/3514228.
- [8] H. V. Gupta, G. S. Nearing, Debates—the future of hydrological sciences: A (common) path forward? Using models and data to learn: A systems theoretic perspective on the future of hydrological science, *Water Resources Research* 50 (6) (2014) 5351–5359. doi:10.1002/2013WR015096.
- [9] M. P. Clark, M. F. P. Bierkens, L. Samaniego, R. A. Woods, R. Uijlenhoet, K. E. Bennett, V. R. N. Pauwels, X. Cai, A. W. Wood, C. D. Peters-Lidard, [The evolution of process-based hydrologic models: historical challenges and the collective quest for physical realism](#), *Hydrology and Earth System Sciences* 21 (7) (2017) 3427–3440. doi:10.5194/hess-21-3427-2017.
URL <https://hess.copernicus.org/articles/21/3427/2017/>
- [10] D. Bolster, K. R. Roche, V. L. Morales, [Recent advances in anomalous transport models for predicting contaminants in natural groundwater systems](#), *Current Opinion in Chemical Engineering* 26 (2019) 72–80. doi:10.1016/j.coche.2019.09.006.
URL <https://www.sciencedirect.com/science/article/pii/S2211339819300413>
- [11] M. Raissi, P. Perdikaris, G. E. Karniadakis, Physics-informed neural networks: A deep learning framework for solving forward and inverse problems involving nonlinear partial differential equations, *Journal of Computational Physics* 378 (2019) 686–707. doi:10.1016/j.jcp.2018.10.045.
- [12] M. Reichstein, G. Camps-Valls, B. Stevens, M. Jung, J. Denzler, N. Carvalhais, Prabhat, [Deep learning and process understanding for data-driven Earth system science](#), *Nature* 566 (7743) (2019) 195–204. doi:10.1038/s41586-019-0912-1.
URL <https://www.nature.com/articles/s41586-019-0912-1>

-
- [13] G. E. Karniadakis, I. G. Kevrekidis, L. Lu, P. Perdikaris, S. Wang, L. Yang, *Physics-informed machine learning*, *Nature Reviews Physics* 3 (6) (2021) 422–440. doi:10.1038/s42254-021-00314-5. URL <https://www.nature.com/articles/s42254-021-00314-5>
- [14] Y. Wu, B. Sicard, S. A. Gadsden, Physics-informed machine learning: A comprehensive review on applications in anomaly detection and condition monitoring, *Expert Systems with Applications* 255 (2024) 124678. doi:10.1016/j.eswa.2024.124678.
- [15] E. de Bézenac, A. Pajot, P. Gallinari, Deep learning for physical processes: Incorporating prior scientific knowledge*, *Journal of Statistical Mechanics: Theory and Experiment* 2019 (12) (2019) 124009. doi:10.1088/1742-5468/ab3195.
- [16] J. Darbon, T. Meng, On some neural network architectures that can represent viscosity solutions of certain high dimensional Hamilton–Jacobi partial differential equations, *Journal of Computational Physics* 425 (2021) 109907. doi:10.1016/j.jcp.2020.109907.
- [17] S. Cuomo, V. S. Di Cola, F. Giampaolo, G. Rozza, M. Raissi, F. Piccialli, Scientific Machine Learning Through Physics-Informed Neural Networks: Where we are and What’s Next, *Journal of Scientific Computing* 92 (3) (2022) 88. doi:10.1007/s10915-022-01939-z.
- [18] A. Arzani, J.-X. Wang, R. M. D’Souza, Uncovering near-wall blood flow from sparse data with physics-informed neural networks, *Physics of Fluids* 33 (7) (Jul. 2021). doi:10.1063/5.0055600.
- [19] G. Kissas, Y. Yang, E. Hwuang, W. R. Witschey, J. A. Detre, P. Perdikaris, Machine learning in cardiovascular flows modeling: Predicting arterial blood pressure from non-invasive 4D flow MRI data using physics-informed neural networks, *Computer Methods in Applied Mechanics and Engineering* 358 (2020) 112623. doi:10.1016/j.cma.2019.112623.
- [20] C. Banerjee, K. Nguyen, C. Fookes, K. George, Physics-Informed Computer Vision: A Review and Perspectives, *ACM Computing Surveys* 57 (1) (2025) 1–38. doi:10.1145/3689037.
- [21] B. A. Toms, E. A. Barnes, I. Ebert-Uphoff, Physically Interpretable Neural Networks for the Geosciences: Applications to Earth System Variability, *Journal of Advances in Modeling Earth Systems* 12 (9) (2020) e2019MS002002. doi:10.1029/2019MS002002.
- [22] W.-P. Tsai, D. Feng, M. Pan, H. Beck, K. Lawson, Y. Yang, J. Liu, C. Shen, From calibration to parameter learning: Harnessing the scaling effects of big data in geoscientific modeling, *Nature Communications* 12 (1) (2021) 5988. doi:10.1038/s41467-021-26107-z.
- [23] C. Shen, A. P. Appling, P. Gentine, T. Bandai, H. Gupta, A. Tartakovsky, M. Baity-Jesi, F. Fenicia, D. Kifer, L. Li, X. Liu, W. Ren, Y. Zheng, C. J. Harman, M. Clark, M. Farthing, D. Feng, P. Kumar, D. Aboelyazeed, F. Rahmani, Y. Song, H. E. Beck, T. Bindas, D. Dwivedi, K. Fang, M. Höge, C. Rackauckas, B. Mohanty, T. Roy, C. Xu, K. Lawson, Differentiable modelling to unify machine learning and physical models for geosciences, *Nature Reviews Earth & Environment* 4 (8) (2023) 552–567. doi:10.1038/s43017-023-00450-9.
- [24] P. Das, A. Posch, N. Barber, M. Hicks, K. Duffy, T. Vandal, D. Singh, K. van Werkhoven, A. R. Ganguly, Hybrid physics-AI outperforms numerical weather prediction for extreme precipitation nowcasting, *npj Climate and Atmospheric Science* 7 (1) (2024) 282. doi:10.1038/s41612-024-00834-8.
- [25] J. Song, Z. Song, P. Ren, N. Benjamin Erichson, M. W. Mahoney, X. S. Li, Forecasting high-dimensional spatio-temporal systems from sparse measurements, *Machine Learning: Science and Technology* 5 (4) (2024) 045067. doi:10.1088/2632-2153/ad9883.
- [26] S. Kim, J. Nathaniel, Z. Hou, T. Zheng, P. Gentine, Spatiotemporal upscaling of sparse air-sea pCO₂ data via physics-informed transfer learning, *Scientific Data* 11 (1) (2024) 1098. doi:10.1038/s41597-024-03959-w.
- [27] S. Jiang, Y. Zheng, D. Solomatine, Improving AI System Awareness of Geoscience Knowledge: Symbiotic Integration of Physical Approaches and Deep Learning, *Geophysical Research Letters* 47 (13) (2020) e2020GL088229. doi:10.1029/2020GL088229.
-

- [28] S. Cuomo, M. De Rosa, F. Giampaolo, S. Izzo, V. Schiano Di Cola, Solving groundwater flow equation using physics-informed neural networks, *Computers & Mathematics with Applications* 145 (2023) 106–123. doi:[10.1016/j.camwa.2023.05.036](https://doi.org/10.1016/j.camwa.2023.05.036).
- [29] D. Secci, V. A. Godoy, J. J. Gómez-Hernández, Physics-Informed Neural Networks for solving transient unconfined groundwater flow, *Computers & Geosciences* 182 (2024) 105494. doi:[10.1016/j.cageo.2023.105494](https://doi.org/10.1016/j.cageo.2023.105494).
- [30] J. D. Hughes, C. D. Langevin, E. R. Banta, Documentation for the MODFLOW 6 framework, Tech. Rep. 6-A57, U.S. Geological Survey (2017). doi:[10.3133/tm6A57](https://doi.org/10.3133/tm6A57).
- [31] A. Vaswani, N. Shazeer, N. Parmar, J. Uszkoreit, L. Jones, A. N. Gomez, L. Kaiser, I. Polosukhin, Attention is All you Need, in: *Advances in Neural Information Processing Systems*, Vol. 30, Curran Associates, Inc., 2017.
- [32] J. Muñoz Sabater, Era5-land hourly data from 1950 to present, copernicus Climate Change Service (C3S) Climate Data Store (CDS) (2019). doi:[10.24381/cds.e2161bac](https://doi.org/10.24381/cds.e2161bac).
- [33] A. Arnab, M. Dehghani, G. Heigold, C. Sun, M. Lucic, C. Schmid, ViViT: A Video Vision Transformer, in: *2021 IEEE/CVF International Conference on Computer Vision (ICCV)*, IEEE, 2021, pp. 6816–6826. doi:[10.1109/ICCV48922.2021.00676](https://doi.org/10.1109/ICCV48922.2021.00676). URL <https://ieeexplore.ieee.org/document/9710415/>
- [34] D. Ulyanov, A. Vedaldi, V. Lempitsky, Instance Normalization: The Missing Ingredient for Fast Stylization (2017). arXiv:[1607.08022](https://arxiv.org/abs/1607.08022), doi:[10.48550/arXiv.1607.08022](https://doi.org/10.48550/arXiv.1607.08022).
- [35] A. Wunsch, T. Liesch, G. Cinkus, N. Ravbar, Z. Chen, N. Mazzilli, H. Jourde, N. Goldscheider, Karst spring discharge modeling based on deep learning using spatially distributed input data, *Hydrology and Earth System Sciences* 26 (9) (2022) 2405–2430. doi:[10.5194/hess-26-2405-2022](https://doi.org/10.5194/hess-26-2405-2022). URL <https://hess.copernicus.org/articles/26/2405/2022/>
- [36] A. Allen, S. Markou, W. Tebbutt, J. Requeima, W. P. Bruinsma, T. R. Andersson, M. Herzog, N. D. Lane, M. Chantry, J. S. Hosking, R. E. Turner, End-to-end data-driven weather prediction, *Nature* (2025) 1–3doi:[10.1038/s41586-025-08897-0](https://doi.org/10.1038/s41586-025-08897-0).
- [37] E. Perez, F. Strub, H. De Vries, V. Dumoulin, A. Courville, FiLM: Visual Reasoning with a General Conditioning Layer, *Proceedings of the AAAI Conference on Artificial Intelligence* 32 (1) (2018). doi:[10.1609/aaai.v32i1.11671](https://doi.org/10.1609/aaai.v32i1.11671).
- [38] E. Vorontsov, C. Trabelsi, S. Kadoury, C. Pal, On orthogonality and learning recurrent networks with long term dependencies, in: *Proceedings of the 34th International Conference on Machine Learning*, PMLR, 2017, pp. 3570–3578.
- [39] N. Bansal, X. Chen, Z. Wang, Can We Gain More from Orthogonality Regularizations in Training Deep Networks?, in: *Advances in Neural Information Processing Systems*, Vol. 31, Curran Associates, Inc., 2018.
- [40] E. Tadmor, A review of numerical methods for nonlinear partial differential equations, *Bulletin of the American Mathematical Society* 49 (4) (2012) 507–554. doi:[10.1090/s0273-0979-2012-01379-4](https://doi.org/10.1090/s0273-0979-2012-01379-4).
- [41] I. Loshchilov, F. Hutter, Decoupled weight decay regularization, in: *Proceedings of the International Conference on Learning Representations (ICLR)*, 2019.
- [42] M. Salis, A. M. Atto, S. Ferraris, R. Meo, Time distributed deep learning models for purely exogenous forecasting: Application to water table depth predictions using weather image time series, *Environmental Modelling & Software* 193 (2025) 106568. doi:<https://doi.org/10.1016/j.envsoft.2025.106568>.
- [43] S. Lee, K.-K. Lee, H. Yoon, Using artificial neural network models for groundwater level forecasting and assessment of the relative impacts of influencing factors, *Hydrogeology Journal* 27 (2) (2019) 567–579. doi:[10.1007/s10040-018-1866-3](https://doi.org/10.1007/s10040-018-1866-3). URL <https://doi.org/10.1007/s10040-018-1866-3>

-
- [44] A. Wunsch, T. Liesch, S. Broda, [Groundwater level forecasting with artificial neural networks: A comparison of long short-term memory \(LSTM\), convolutional neural networks \(CNNs\), and non-linear autoregressive networks with exogenous input \(NARX\)](#), *Hydrology and Earth System Sciences* 25 (3) (2021) 1671–1687. doi:10.5194/hess-25-1671-2021. URL <https://hess.copernicus.org/articles/25/1671/2021/>
- [45] R. B. Cleveland, W. S. Cleveland, I. Terpenning, STL: A Seasonal-Trend Decomposition Procedure Based on Loess, *Journal of Official Statistics* (1990) 3–73.
- [46] X. Wang, K. Smith, R. Hyndman, Characteristic-Based Clustering for Time Series Data, *Data Mining and Knowledge Discovery* 13 (3) (2006) 335–364. doi:10.1007/s10618-005-0039-x.
- [47] W. Fedus, B. Zoph, N. Shazeer, Switch transformers: Scaling to trillion parameter models with simple and efficient sparsity, *J. Mach. Learn. Res.* 23 (1) (2022) 120:5232–120:5270.
- [48] R. T. Q. Chen, Y. Rubanova, J. Bettencourt, D. K. Duvenaud, Neural Ordinary Differential Equations, in: *Advances in Neural Information Processing Systems*, Vol. 31, Curran Associates, Inc., 2018.
- [49] M. Buchhorn, M. Lesiv, N.-E. Tsendbazar, M. Herold, L. Bertels, B. Smets, Copernicus global land service: Land cover 100 m: Collection 3: epoch 2019: Globe, Zenodo (2020). doi:10.5281/zenodo.3939050.
- [50] P. O'Neill, S. Chan, E. Njoku, T. Jackson, R. Bindlish, J. Chaubell, [Smmap enhanced l3 radiometer global daily 9 km ease-grid soil moisture, version 4](#) (2020). doi:10.5067/NJ34TQ2LFE90. URL http://nsidc.org/data/SPL3SMP_E/versions/4